

THE ZURICH ENVIRONMENTAL STUDY OF GALAXIES IN GROUPS ALONG THE COSMIC WEB. III. GALAXY PHOTOMETRIC MEASUREMENTS AND THE SPATIALLY RESOLVED COLOR PROPERTIES OF EARLY- AND LATE-TYPE SATELLITES IN DIVERSE ENVIRONMENTS*

A. CIBINEL¹, C. M. CAROLLO¹, S. J. LILLY¹, S. BONOLI², F. MINIATTI¹, A. PIPINO¹, J. D. SILVERMAN³, J. H. VAN GORKOM⁴,
E. CAMERON¹, A. FINOGUENOV⁵, P. NORBERG⁶, Y. PENG¹, AND C. S. RUDICK¹

¹ Institute of Astronomy, ETH Zurich, CH-8093 Zurich, Switzerland; cibinel@phys.ethz.ch, marcella@phys.ethz.ch

² Institute for Theoretical Physics, University of Zürich, Winterthurerstrasse 190, CH-8057 Zürich, Switzerland

³ Kavli Institute for the Physics and Mathematics of the Universe (WPI), Todai Institutes for Advanced Study, The University of Tokyo, 5-1-5 Kashiwanoha, Kashiwa 277-8583, Japan

⁴ Department of Astronomy, Columbia University, New York, NY 10027, USA

⁵ Max-Planck-Institut für extraterrestrische Physik, D-84571 Garching, Germany

⁶ Institute for Computational Cosmology, Department of Physics, Durham University, South Road, Durham DH1 3LE, UK

Received 2012 June 14; accepted 2013 August 27; published 2013 October 21

ABSTRACT

We present photometric measurements for the galaxies—and when possible their bulges and disks—in the $0.05 < z < 0.0585$ groups of the Zurich Environmental Study (ZENS); these measurements include $(B - I)$ colors, color gradients and maps, color dispersions, as well as stellar masses and star formation rates. The ZENS galaxies are classified into quenched, moderately star-forming, and strongly star-forming using a combination of spectral features and far-UV-to-optical colors; this approach optimally distinguishes quenched systems from dust-reddened star-forming galaxies. The latter contribute up to 50% to the $(B - I)$ “red sequence” at $\sim 10^{10} M_{\odot}$. At fixed morphological or spectral type, we find that galaxy stellar masses are largely independent of environment, and especially of halo mass. As a first utilization of our photometric database, we study, at fixed stellar mass and Hubble type, how $(B - I)$ colors, color gradients, and color dispersion of *disk satellites* depend on group mass M_{GROUP} , group-centric distance R/R_{200} , and large-scale structure overdensity δ_{LSS} . The strongest environmental trend is found for *disk-dominated satellites* with M_{GROUP} and R/R_{200} . At $M \lesssim 10^{10} M_{\odot}$, disk-dominated satellites are redder in the inner regions of the groups than in the outer parts. At $M \gtrsim 10^{10} M_{\odot}$, these satellites have shallower color gradients in higher mass groups and in the cores of groups compared with lower mass groups and the outskirts of groups. Stellar population analyses and semi-analytic models suggest that disk-dominated satellites undergo quenching of star formation in their outer disks, on timescales $\tau_{\text{quench}} \sim 2$ Gyr, as they progressively move inside the group potential.

Key words: catalogs – galaxies: evolution – galaxies: groups: general – galaxies: photometry – galaxies: star formation – surveys

Online-only material: color figures

1. INTRODUCTION

A key open question in galaxy evolution is which of the many characteristics of a given galaxy’s “environment” most strongly affects its ability to form new stars. Different environments that galaxies experience vary from conditions within their host group/cluster halo (related to the total mass of the halos), to their precise location within these halos (related to the distance from the group/cluster center), to their rank within halos as central or satellite galaxies, to the underlying density field of the cosmic large-scale filamentary structure (LSS). All these different aspects of environment may be in principle important.

To make headway in understanding which environment has an impact on galactic evolution, we have undertaken the Zurich Environmental Study (ZENS; Carollo et al. 2013, hereafter Paper I), a comprehensive study of detailed galaxy properties as a function of group halo mass, projected group-centric distance, LSS density, and central/satellite ranking within the group potentials. ZENS uses the same local galaxy sample to perform the environment-versus-environment comparisons, which eliminates any bias when interpreting the results. Detailed

structural properties for the ZENS galaxies and their bar, bulge, and disk components have been presented in Cibinel et al. (2013, hereafter Paper II). In this third paper in the ZENS sequence we focus on photometric galactic diagnostics, such as stellar masses and star formation rates (SFRs).

The history of the growth of stellar mass in the universe is imprinted in the properties of star-forming and passively evolving (or, better, “quenched”) galaxy populations at different epochs and, at each epoch, in different environments. Many works have suggested that high SFRs are rarer in dense environments, and that galaxy groups and clusters may host a higher fraction of quenched early-type galaxies relative to the field (e.g., Oemler 1974; Dressler 1980; Balogh et al. 2004; Croton et al. 2005). Relatively recently, however, with the advent of large spectroscopic surveys such as the 2dFGRS (Colless et al. 2001) and the Sloan Digital Sky Survey (SDSS; York et al. 2000) at low redshifts, and others at high redshifts (e.g., zCOSMOS, Lilly et al. 2007, 2009; DEEP2, Davis et al. 2005; Newman et al. 2013), it has become clear that galaxy properties, including SFRs, strongly depend on galaxy stellar mass (e.g., Brinchmann et al. 2004; Tremonti et al. 2004; Baldry et al. 2006; van der Wel 2008; Peng et al. 2010). This requires that environmental effects are carefully disentangled from those of galaxy mass both in the implementation and in the interpretation of observational studies.

* Based on observations collected at the European Southern Observatory, La Silla Chile. Program ID 177.A-0680.

Analyses of the SDSS have suggested that, over about two dex of galaxy mass, the fraction of red galaxies rises with increasing environmental density (Baldry et al. 2006; Bamford et al. 2009; measured, however, through a proxy that is degenerate with group-centric distance; see Paper I; Peng et al. 2012; Woo et al. 2013). Woo et al. (2013) have furthermore shown that the fraction of quenched galaxies appears more strongly correlated with halo mass at fixed galaxy stellar mass than vice versa. The interpretation of those results is, however, made fuzzy by the fact that they can be explained, at least qualitatively, in terms of a hierarchical increase in halo mass, without an increase in stellar mass for quenched objects. There is furthermore evidence that the galaxy mass function may vary itself with local environmental density (Baldry et al. 2006; Bundy et al. 2006; Bolzonella et al. 2010; Kovač et al. 2010).

Based on a phenomenological approach to galaxy evolution that is constructed around the basic continuity equation for galaxies, Peng et al. (2010) have shown that the quenching transition of galaxies from the blue cloud to the red sequence is due to a fully separable combination of two processes, one linked to the stellar mass of a galaxy (or a proxy), independent of the environment, and the other linked to the environment, independent of the galaxy stellar mass. The former “mass-quenching” process dominates at high stellar masses above $\sim 10^{10.5} M_{\odot}$ and has a rate proportional to the SFR; it is this process that seems to control the mass functions of both active and quenched galaxies. The second “environment-quenching” process dominates at lower stellar masses (Peng et al. 2012). Which physics is responsible for mass quenching and environment quenching is still debated.

A number of studies have postulated the existence of a typical halo mass scale, of about $10^{12} M_{\odot}$, above which the interplay between shock heating and feedback from, e.g., active galactic nuclei (AGNs) makes the cooling of the intergalactic medium and subsequent star formation progressively inefficient (e.g., Dekel & Birnboim 2006; Cattaneo et al. 2006; Khochfar & Ostriker 2008; Cen 2011). Others have highlighted a possible environmental dependence of the halo assembly histories as the origin of the relation between galaxy star formation activity and environment (e.g., Sheth & Tormen 2004; Gao et al. 2005; Maulbetsch et al. 2007; Hahn et al. 2007, 2009; Crain et al. 2009).

Peng et al. (2012) find that their environment quenching in the general galaxy population is confined to processes acting on the satellite population (i.e., their environment quenching is a “satellite-quenching” process); the fraction of satellite galaxies that experience such quenching in their analysis ranges from 30% to 75%, depending on the local density, but not at all on halo mass (above $10^{12} M_{\odot}$). This indicates that environmental effects may thus be relevant as galaxies enter group-sized halo potentials and there become satellites of the central galaxy. Analyses of SDSS groups have shown that, at fixed stellar mass, satellites in groups are indeed on average redder than central galaxies (van den Bosch et al. 2008; Skibba 2009; Weinmann et al. 2009). An analysis of groups out to $z \simeq 0.8$ in the zCOSMOS field demonstrated that such difference between central and satellite galaxies is still observed also at these higher redshifts (Knobel et al. 2012). Within a cold dark matter (CDM) framework, suppression of star formation in galaxies once these are accreted into bigger halos may happen, e.g., due to ram-pressure stripping of their cold gas (Gunn & Gott 1972) or removal of their hot gas (Larson et al. 1980; Balogh et al. 2000).

The precise mass scale at which halo physics may start influencing the star formation properties of satellite galaxies is, however, not well known. Numerical simulations show that galaxies are depleted of their cold and hot gas as they enter the virialized regions of relatively small groups (e.g., Kawata & Mulchaey 2008; Feldmann et al. 2011). Peng et al. (2012) have argued that many of the key evolutionary processes on satellites, namely, the specific star formation rates (i.e., $\text{SFR}/M_{\text{galaxy}}$; sSFR) of star-forming galaxies, the mass-quenching process, and the environment quenching (at fixed density) are all strikingly independent of halo mass above $10^{12} M_{\odot}$. Galaxies may thus be quenched as they become satellites in small groups, well before these assemble into larger cluster-sized structures.

Observational diagnostics that have been heavily studied to understand how star-forming galaxies are transformed into red-and-dead stellar systems have been typically limited to integrated galaxy properties (e.g., total galaxy colors and SFRs). Also, morphological analyses of the satellite and central galaxy populations have been typically based on a separation into early- and late-type galaxies by means of a threshold in either galaxy concentration or Sérsic index n (Sersic 1968), which leads to mixing of galaxies with very different bulge-to-disk ratios, arguably the most physical diagnostics to classify galaxy structure and morphology (see Paper II).

Open questions thus remain whether and how the strength of environmental effects varies between galaxy populations with different bulge-to-disk ratios, and whether and to what extent the environmental forcing affects differentially the bulge or disk components of galaxies. To test the different physical scenarios, it is furthermore imperative that, in addressing these questions, the different aspects of the environment of a galaxy are carefully disentangled. We will directly tackle these issues in a number of forthcoming ZENS papers.

In the present third paper in the ZENS sequence, we introduce the methodology adopted to measure the photometric properties of ZENS galaxies and the tests that we have performed to assess the impact of systematic errors on these properties. The photometric measurements include galaxy SFRs, stellar masses, colors, color gradients, and two-dimensional color maps as well as, e.g., bulge/disk colors and masses, etc. With the purpose of presenting a simple first utilization of these photometric measurements (coupled with the structural galaxy measurements of Paper II and with the environmental diagnostics of Paper I), we also discuss the $(B - I)$ colors and color gradients of *satellite* galaxies as a function of galaxy mass at constant Hubble type, and of group halo mass, group-centric distance and LSS density.

After a brief summary of ZENS in Section 2, this paper is structured as follows. The bulk of the paper describes the photometric analyses performed on the ZENS galaxy sample: stellar masses, both for the entire galaxies and their bulge and disk components, and mass completeness limits, are derived using synthetic templates and broad-band photometry in Sections 3 and 4. Section 5 presents the criteria that we have used to classify strongly and moderately star-forming galaxies, and quenched galaxies, based on the combination of spectral features, far- and near-UV (FUV/NUV) versus optical colors, and fits to the galaxy spectral energy distributions (SEDs). We also highlight in this section the importance of the comparison of multiple star formation diagnostics, to avoid misclassifications in the spectral types of galaxies. We discuss the derivation and associated systematic biases of resolved color maps and radial color profiles in Section 6. Section 7 analyses, above our stellar mass completeness limits, variations in median galaxy stellar mass of satellites

and centrals as a function of group mass, group-centric distance and LSS density. Section 8 shows the dependence of colors, color gradients and color scatter at fixed stellar mass for the different Hubble types determined in Paper II. Section 9 presents our first environmental study of the presented measurements, i.e., the dependence of colors, color gradients and color scatter in *disk satellites* on the different environmental parameters. We summarize the paper in Section 10. In the Appendix we provide supplementary information on the tests we performed to assess the reliability of galaxy properties derived from our SED fits. Throughout the paper we will assume the following values for the relevant cosmological parameters: $\Omega_m = 0.3$, $\Omega_\Lambda = 0.7$ and $h = 0.7$. Magnitudes are in the AB system (Oke 1974).

We remind the reader that all measurements for the 1484 galaxies in the 141 ZENS groups are made public in the ZENS catalog⁷ published with Paper I.

2. A SUMMARY OF ZENS

ZENS uses 141 groups of galaxies selected from the 2dFGRS Percolation-Inferred Galaxy Group (2PIGG) catalog (Eke et al. 2004). The groups were randomly selected from all groups in the 2PIGG catalog which are located at $0.05 < z < 0.0585$ and have at least five spectroscopically confirmed galaxy members. New *B*- and *I*-band observations were taken with the Wide Field Imager (WFI) camera mounted at the MPG/ESO 2.2 m telescope, reaching a background-limited depth of $\mu(B) = 27.2$ mag arcsec⁻² and $\mu(I) = 25.5$ mag arcsec⁻² over an area of 1 arcsec².

In ZENS we focus our attention on the following measures of galactic environment:

1. the mass of the group halo in which galaxies reside, M_{GROUP} ;
2. the distance of a galaxy from the center of the host group, normalized to the characteristic group radius R_{200} ;
3. the large scale (over)density field δ_{LSS} , quantified through the overdensity of 2PIGG *groups* at the ZENS field positions, within a circular projected area of size equal to the comoving distance to the fifth nearest 2PIGG group, i.e., $\delta_{\text{LSS}} = ((\rho_{\text{LSS}}(z) - \rho_m)/\rho_m)$ (with $\rho_{\text{LSS}}(z)$ the density of 2PIGG groups out to the fifth nearest neighboring group, and ρ_m the mean projected density in the 2dFGRS volume); and
4. the rank of the galaxy within the host group, i.e., whether the galaxy is the central galaxy or a satellite galaxy in orbit around the central.

Attention was paid to ascertain whether the ranking of galaxies as centrals and satellites led to a self-consistent solution for the central galaxies (required to be the most massive, within the errors on the estimated stellar masses, as well as compatible with being the geometrical and velocity centroids of the groups). Groups with a well-identified central galaxy were defined as “relaxed,” while groups in which no galaxy member satisfied all requirements to be considered a central galaxy were defined to be “unrelaxed.”

We refer to Paper I for further details on the ZENS sample and our environmental definitions and to Paper II for details on the structural measurements and morphological classification of the ZENS galaxies, as well as on the data reduction and calibration of the WFI data.

⁷ The ZENS catalog is also downloadable from <http://www.astro.ethz.ch/research/Projects/ZENS>.

Table 1
Fraction of ZENS Galaxies with Available Multi-band Photometry

Band	Coverage
FUV, NUV (<i>GALEX</i>)	89%
<i>B</i> , <i>I</i> (ESO/WFI)	100%
<i>u</i> , <i>g</i> , <i>r</i> , <i>i</i> , <i>z</i> (SDSS)	29%
<i>J</i> , <i>H</i> , <i>K</i> (2MASS)	98%

Note. The fraction of ZENS galaxies with available photometric data from the listed surveys.

3. STELLAR MASSES FOR THE ZENS GALAXIES

To estimate the stellar masses (hereafter M_{galaxy} or, when unambiguous, simply M for simplicity) for the ZENS galaxies, we fitted synthetic spectral templates to their broadband photometric data. To this end we employed our code ZEBRA+ (The Zurich Extragalactic Bayesian Redshift Analyzer Plus; Oesch et al. 2010), an upgrade of the public version of the ZEBRA package presented in Feldmann et al. (2006). Relative to ZEBRA, the upgraded ZEBRA+ code enables the use of synthetic templates for the estimation of stellar masses, ages, and metallicities. In the following we describe in detail the photometric data and the model templates used to derive the galaxy stellar masses.

3.1. Photometry

In order to constrain at best the template fits, we combined all available photometry for the sample galaxies, including our new WFI *B* and *I* imaging data as well as data from the literature. Specifically, for each galaxy we used, when available, SDSS *u*, *g*, *r*, *i*, *z* (Abazajian et al. 2009), Two Micron All Sky Survey (2MASS) *J*, *H*, *K* (Skrutskie et al. 2006), and *Galaxy Evolution Explorer* (*GALEX*; Martin et al. 2005), near-UV (NUV) and far-UV (FUV) magnitudes. The fraction of ZENS galaxies with observations at any given wavelength is summarized in Table 1.

We calibrated the data products from these surveys following the instructions provided by the respective teams. For the SDSS we used the legacy imaging data with the “best” reduction from the Data Release 7 (DR7), and for 2MASS we use the Atlas data product. In the case of *GALEX* we used the GR6 All-sky Survey (AIS) tiles or, when available, the deeper Medium Survey intensity (MIS) maps. In the case of more than one AIS observation, we used the data having the longer exposure time.

We measured the magnitudes in all passbands using an elliptical aperture equal to $2 \times R_{p_{\text{MAX}}}$, with $R_{p_{\text{MAX}}}$ the larger of the two Petrosian semi-major axes R_{p_I} and R_{p_B} measured with SExtractor (Bertin & Arnouts 1996) on the WFI *I*- and *B*-band images. When available we used the sky-background estimates or maps provided by the survey pipelines; otherwise, the background was subtracted using the mode of the intensity in the pixels located outside the Petrosian aperture. A comparison between the fluxes we measured and those found in the survey’s public catalogs is shown in Figure 18 of the Appendix, together with a discussion on possible biases arising from differences in the average point-spread function (PSF) in the different passbands.

All the magnitudes were corrected for galactic extinction using $E(B - V)$ values from the survey catalogs, if provided, or obtained from the dust maps of Schlegel et al. (1998), assuming a Cardelli et al. (1989) extinction law. For correcting *GALEX* magnitudes, we applied the relations $A_{\text{FUV}}/E(B - V) = 8.376$ and $A_{\text{NUV}}/E(B - V) = 8.741$ as derived by Wyder et al. (2005).

2MASS magnitudes were converted into the AB system by applying the following transformations, which we calculated using the IRAF package *synphot* and the composite Vega spectrum released by STSCI⁸: $J_{AB} = J_{VEGA} + 0.894$, $H_{AB} = H_{VEGA} + 1.367$, and $K_{AB} = K_{VEGA} + 1.837$.

Before calculating the masses, we ran ZEBRA+ in the *photometry-check mode* in order to correct for possible systematics in the calibration of the input catalog. With this option it is possible to detect residuals between the best-fit template and the galaxy fluxes that are independent of template type itself (see Feldmann et al. 2006 for more details). This check revealed that there was a small offset in the SDSS *i* and *z* bands equal to -0.03 and 0.04 mag, respectively. We applied these small shifts to the SDSS *i* and *z* band before proceeding to the derivation of masses for our galaxies.

3.2. Synthetic Template Library

To model the SED of the ZENS galaxies, we used a set of Bruzual & Charlot (2003, hereafter BC03) synthetic models with a Chabrier (2003) initial mass function (IMF), truncated at $0.1 M_{\odot}$ and $100 M_{\odot}$ and based on the Padova 1994 evolutionary tracks. We used star formation histories (SFHs) described by exponentially declining SFRs $\psi(t) = \psi_0 \tau^{-1} e^{-t/\tau}$, with different values for the characteristic time τ , as well as by a constant SFR (CSF, $\tau \rightarrow \infty$). The normalization factor ψ_0 was set to 1 by imposing a total mass of $1 M_{\odot}$ at time $t \rightarrow \infty$. Each SFH was sampled with 900 templates of metallicities Z ranging between 0.004 ($1/5 Z_{\odot}$) and 0.04 ($2 Z_{\odot}$) and ages between 10 Myr and 12 Gyr.

Reddening produced by dust was also taken into account: a dust correction was allowed in the ZEBRA+ fits and often required for galaxies morphologically classified as spirals or irregular. The dust extinction was assumed to be described by a Calzetti et al. (2000) relation, and the corresponding reddening $E(B - V)$ was allowed to vary between 0 and 0.5, in 27 fine steps. A substantial dust attenuation, $E(B - V) > 0.25$, was permitted only for star-forming templates, i.e., templates with $\text{age}/\tau < 4$ (see also Pozzetti et al. 2007; Ilbert et al. 2010), and for galaxies not spectrally classified as “quenched” (see Section 5). Galaxies with a best-fit template with $\text{age}/\tau > 4$ and $E(B - V) > 0.25$ were fitted using a dust grid with a maximum value of $E(B - V) = 0.25$. Galaxies morphologically classified as elliptical and S0 required no dust in their SED fits. A complete summary of the parameter space covered by the adopted templates is presented in Table 2. Knowing the spectroscopic redshift of our galaxies, we ran ZEBRA+ in the maximum likelihood mode keeping the redshift fixed to the right values. The best-fit templates from ZEBRA+ were also used to compute the *k*-correction for each galaxy. At the redshift of the ZENS groups, the *k*-corrections are small but not negligible: in *B* band these are typically 0.15 mag, and they increase up to 0.3 mag in the NUV, depending on the galaxy intrinsic SED (see also Blanton & Roweis 2007).

SFRs were computed as $\text{SFR} = M_{\text{galaxy}}/t_A$ for constant SFR models and $\text{SFR} = (M_{\text{galaxy}}/(1 - e^{-t_A/\tau}))(e^{-t_A/\tau}/\tau)$ for exponentially declining SFHs (with t_A the age of the best-fit model).

In our ZENS analyses we will adopt as or fiducial estimates for the stellar masses those obtained from the integration of the galaxies’ SFRs. We estimate that the “actual” stellar masses, which are obtained by removing the fraction of mass that is

Table 2

Template Library Used to Derive Stellar Masses and (s)SFRs with ZEBRA+

Parameter	Range of Values
Z	0.004, 0.007, 0.01, 0.02 (Z_{\odot}), 0.03, 0.04
τ (Gyr)	0.05, 0.1, 0.3, 0.6, 1, 1.5, 2, 3, ..., 10, ∞
Age (Gyr)	0.01–12
$E(B - V)$	0–0.5

Notes. The properties of the synthetic spectra used to derive galaxy stellar masses and SFRs through fits to the galaxy SEDs. From top to bottom: metallicity, exponentially declining SFH timescale, stellar age (sampled in 150 logarithmic bins), and dust reddening (sampled in 27 steps, spaced by 0.01 mag in the range $E(B - V) = 0 \rightarrow 0.1$ and by 0.025 mag at higher reddening). Values of dust extinction $E(B - V) > 0.25$ were allowed only in models with $\text{age}/\tau < 4$ for galaxies classified as non-quenched (see Section 5).

returned to the interstellar medium (ISM) by the dying stars, are on average smaller by about -0.2 dex than the adopted “integrated” stellar masses. An assessment of the uncertainty and reliability of the masses derived with ZEBRA+ is given in the Appendix, where we compare our results with previously published data and present further considerations on other possible systematics.

3.3. Mass Completeness of the ZENS Galaxy Sample

Given the apparent magnitude selection of the 2dFGRS and the 2PIGG group catalog, the raw ZENS galaxy sample is not a mass-complete sample: the $b_j \lesssim 19.45$ mag limit of the survey translates into a minimum observed mass that depends on the intrinsic SED of the galaxies and is thus different for different galaxy types. Galaxies with the highest mass-to-light ratio (M/L) thus set the mass completeness limit of our survey. We infer this limit empirically from the observed M/L of the ZENS galaxies, following an approach similar to that described in Pozzetti et al. (2010). Specifically, for each galaxy we compute the mass that it would have, given its M/L, once reduced in brightness to the survey limiting magnitude, i.e., $\log(M_{\text{lim}}) = \log(M) + 0.4(b_j - b_{j,\text{lim}})$. As discussed in Pozzetti et al. (2010), deriving the mass limits using the entire galaxy sample can lead to values that are too conservative and not representative of the masses of the typical galaxies with luminosity close to the survey limit. For each morphological or spectral galaxy type we therefore used the 30% faintest galaxies to calculate the completeness mass. This is defined as the mass below which lie 85% of the M_{lim} for the faint galaxies, i.e., the mass *above* which 85% of these galaxies still fulfill the criterion $b_j < 19.45$. This is illustrated in Figure 1 for the three galaxy spectral types in which we have classified our ZENS sample in Section 5.

The resulting completeness limits are, precisely, $\log(M/M_{\odot}) > 9.90$, $\log(M/M_{\odot}) > 9.78$, and $\log(M/M_{\odot}) > 9.24$ for quenched, moderately star-forming, and strongly star-forming galaxies respectively. Folding in the statistical mix of spectroscopic type in our morphological bins (defined in Paper II), the mass completeness limits for galaxies of different morphological types are $\log(M/M_{\odot}) > 10.04$ for E/S0 galaxies, $\log(M/M_{\odot}) > 9.93$ for bulge-dominated spiral galaxies, $\log(M/M_{\odot}) > 9.78$ for intermediate spirals, and $\log(M/M_{\odot}) > 9.55$ for late spirals and irregulars. In the rest of this paper we will homogenize these limits and use $M = 10^{10} M_{\odot}$ as the mass limit for the spectral and morphological early-type galaxies and $M = 10^{9.5} M_{\odot}$ for star-forming and morphological late-type galaxies.

⁸ <http://www.stsci.edu/hst/observatory/cdbs/calspec.html>

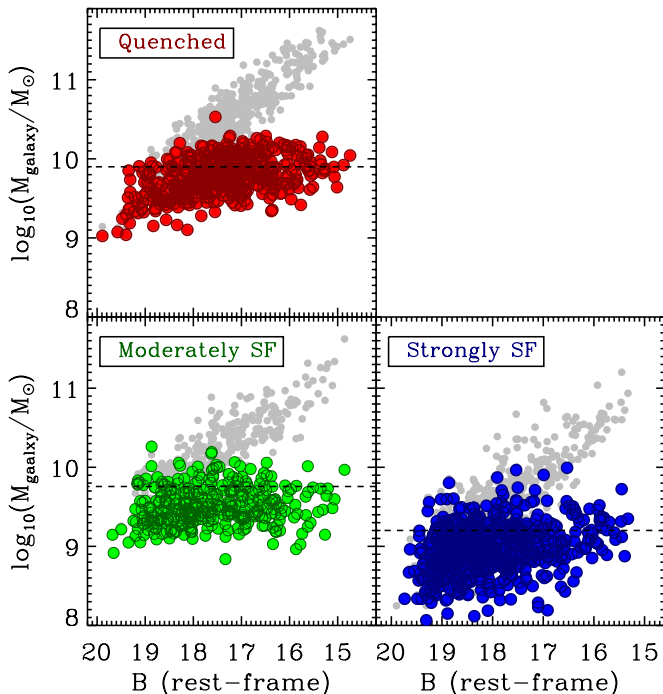


Figure 1. Illustration of the mass completeness derivation for galaxies of the three different spectral types defined in Section 5. The panels show galaxy stellar mass as a function of apparent B -band magnitude, separately for quenched, moderately star-forming, and strongly star-forming galaxies. Small gray dots are galaxy masses inferred from the ZEBRA+ best fits to the photometric data of ZENS galaxies; large black symbols (colored in the online version) show the stellar masses $\log(M_{\text{lim}}) = \log(M) + 0.4(b_j - b_{j,\text{lim}})$ obtained by fading galaxies to the 2dFGRS limiting magnitude (red, green, and blue are respectively used for quenched, moderately star-forming, and strongly star-forming galaxies in the online version). The dashed horizontal lines mark the mass completeness limits, defined, separately for each spectral type, as the mass below which lie 85% of the M_{lim} for the 30% faintest galaxies of that given type (see text).

(A color version of this figure is available in the online journal.)

We finally stress that, as a consequence of their definition and of our ZENS sample selection, the distributions of galaxy masses for central and satellite galaxies over the common mass range are substantially different, as shown explicitly in Figure 2; furthermore, these two populations overlap basically only at mass scales $\sim 10^{10} - 10^{10.7} M_{\odot}$. We will thus take this bias into account when comparing the properties of centrals and satellites in our ZENS studies.

4. DERIVATION OF STELLAR MASSES FOR THE BULGES AND DISKS OF TWO-COMPONENT GALAXIES

In addition to deriving the stellar masses for the entire galaxies as described above, we also estimated stellar masses separately for the bulge and disk components of disk galaxies with bulge/disk decompositions available from Paper II through GIM2D (Simard et al. 2002) decompositions. To this purpose, we converted the $(B - I)$ colors of bulges and disks into an I -band M/L by using a set of stellar population models from the BC03 library, constructed with a Chabrier IMF. We adopted as our fiducial M/L for the galaxy components the median M/L obtained from fitting all the synthetic spectra.

We employed simple stellar population (SSP) models, as well as exponentially decreasing SFHs, with characteristic timescales of $\tau = 1, 3, 6$ Gyr. For each SFH we used the range of metallicities $Z = 0.004, 0.005, 0.008, 0.01, 0.02, 0.03, 0.05$, in units such that 0.02 is the solar metallicity (Z_{\odot}). Another set

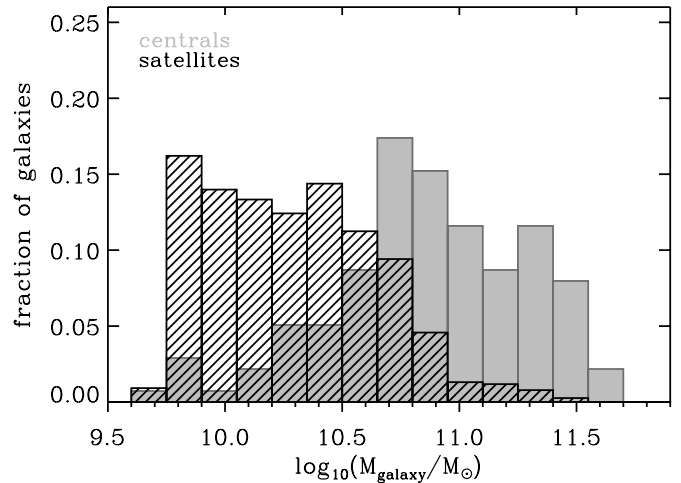


Figure 2. Distributions of galaxy stellar masses for central (filled gray histogram) and satellite galaxies (black hatched histogram), over the mass range spanned by the central population. Each histogram is normalized to its sum.

of models, based on the same grid of parameters, was reddened with a Calzetti dust law and $E(B - V) = 0.05, 0.1, 0.15, 0.2, 0.4, 0.5$. Dust-reddened models with $E(B - V) > 0.2$ were used only for galaxies classified as dusty star-forming (see Section 5).

A k correction is needed to convert the bulge and disk apparent magnitudes into rest-frame luminosities. Whereas for the entire galaxies we can calculate these corrections from the UV to near-infrared (NIR) SED fits of ZEBRA+, such information is not available for the bulges and disks for which we have only the B - and I -band photometry. For this reason, we performed a linear fit to the relation between the apparent $(B - I)$ color and the ZEBRA+ k corrections as obtained for the entire galaxies, and we used this average relation to infer the k corrections for the galaxy components. Consistently with the definition adopted for the galaxies, we consider in the following total stellar masses for bulges and disks, which include also the fraction of baryons that is returned as gas to the ISM as stars evolve.

To assess the reliability of the derived masses of bulges and disks, in Figure 3 we compare the total galaxy stellar masses derived in Section 3 with the sum of the stellar masses of their bulge and disk components. We highlight with red and blue symbols, respectively, elliptical galaxies and pure disk galaxies, i.e., galaxies for which a two-component GIM2D fit returns as the best fit a model with $B/T = 0$. The figure shows a very good agreement with a scatter of ~ 0.2 dex, comparable with the average error on the total galaxy mass estimate (see the Appendix).

5. DEFINITION OF GALAXY SPECTRAL TYPES: QUENCHED, MODERATELY STAR-FORMING, AND STRONGLY STAR-FORMING GALAXIES

The split between quenched and star-forming galaxies is a rather arbitrary one, for many reasons. First, it is plausible to expect that, in nature, star formation activity is a continuum property of galaxies, and the distinction between the two populations is not a dichotomy. Second, observational biases such as threshold of detectability of SFRs in any given survey can affect the classification. In ZENS we try to clean, as much as possible, our quenched/star-forming classification of galaxies in the sample, by adopting an approach that combines three different probes of star formation activity, namely,

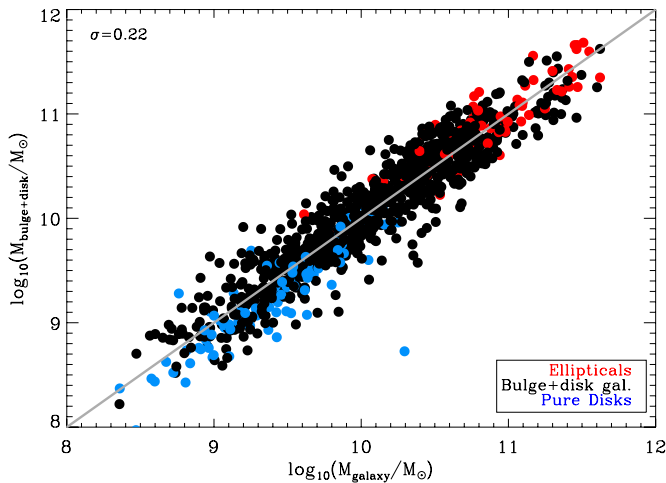


Figure 3. Comparison between galaxy stellar masses derived from the SED fits to the galaxies photometric data and galaxy stellar masses obtained by summing up the separate contributions of their bulges and disks. Bulge and disk stellar masses are inferred from the GIM2D bulge+disk decompositions of Paper II, using the $(B - I)$ colors of these components as proxies for their M/L values ($(B - I)$ colors from the single Sérsic fits are used for elliptical galaxies). Elliptical galaxies are shown in black (red in the online version), and single-exponential (i.e., “pure”) disk galaxies in dark gray (blue in the online version); galaxies with both a bulge and a disk component are shown in gray (black in the online version). The two mass estimates show a very good agreement within a scatter of $\sigma = 0.22$ dex.

(A color version of this figure is available in the online journal.)

(1) the original 2dF spectra, (2) FUV–NUV–optical colors, and (3) the SFR estimates from the SED fits to the galaxy photometry described above. The main philosophy that we adopt is to automatically classify a galaxy as star-forming or quenched when all three diagnostics agree on the classification, and to explore all diagnostics to understand what causes discrepancies when these arise. We end up with a three-bin classification in quenched, moderately star-forming, and strongly star-forming galaxies, the last two classes being broadly diversified by the level of the sSFR measured by the SED fits. We detail our classification procedure below.

5.1. First Constraint to the Spectral Classification: Line Features in the 2dFGRS Spectra

The 2dFGRS team provides for each galaxy the spectral indicator η (Madgwick et al. 2002), which characterizes the activity of the galaxy. The parameter η correlates by definition with the intensity of the emission lines (most strongly with the equivalent width of $H\alpha$); however, it does not contain detailed information on which species are in emission nor their relative strength, aspects that are important to identify mixed types or galaxies in which the emission is powered by an AGN rather than by star formation. Furthermore, we worried that the fibers of the 2dFGRS spectrograph, having a fixed diameter of $2''$ – $2''.16$, probe a different fraction of the galaxy light depending on the galaxy’s apparent radius. Whereas for a good fraction of the ZENS galaxies the $2''$ aperture is large enough to cover a significant part of the galaxy, for others the spectrum is only probing the innermost region, leaving scope for misclassifications. We thus individually inspected the 2dFGRS spectra of the ZENS galaxies to study the emission and absorption line features in the galaxy spectra.

A relative flux calibration for the spectra was obtained by using the average response function and telluric corrections

available on the 2dFGRS Web site.⁹ A boxcar-averaged continuum (over 250 pixels) was subtracted from the spectra before performing the visual inspection. The wide wavelength coverage of the 2dFGRS spectra and the low redshifts of our galaxies allow us to look for a number of star formation tracers, i.e., hydrogen $H\beta$ and $H\alpha$ Balmer lines, and forbidden transitions of $[O\text{II}] \lambda 3727$, $[O\text{III}] \lambda 5007$, and $[N\text{II}] \lambda 6584$.

Based on the spectral information, we classified a galaxy as *quenched* if its spectrum satisfies one of the following conditions: (1) none of the aforementioned lines are observed in emission or (2) some $[O\text{II}]/[N\text{II}]$ emission is present but no $H\beta$ or $H\alpha$ is detected. It is not unusual to observe $[O\text{II}]$ or $[N\text{II}]$ emission in ellipticals or in galaxies on the red sequence (e.g., Caldwell 1984; Phillips et al. 1986; Macchetto et al. 1996), but the presence of this ionized gas is often a consequence of AGNs or excitation in low-ionization nuclear emission-line regions rather than a signature of star formation spread across the entire galaxy (Yan et al. 2006; Annibali et al. 2010; Lemaux et al. 2010).

Galaxies were classified as star-forming if they showed emission in the above species, particularly $H\beta$ and/or $H\alpha$. Emission-line spectra can have, however, large contributions from AGNs (Heckman 1980; Baldwin et al. 1981; Veron et al. 1997; Kauffmann et al. 2003a). A widely used method to identify AGNs, first proposed by Baldwin et al. (1981) and revised in several later works (e.g., Veilleux & Osterbrock 1987; Tresse et al. 1996), relies on the relative strength of the $[N\text{II}]/H\alpha$ and $[O\text{III}]/H\beta$ line ratios. We used this diagnostic to identify AGN candidates in our sample; in these galaxies, the classification in quenched or star-forming systems relied entirely on the color–color criteria.

In the next section we describe how we further split star-forming galaxies into two classes of, respectively, *strongly star-forming* and *moderately star-forming* systems. The latter identify a transition galaxy type with modest star formation activity in between that of strongly star-forming and quenched galaxies. This transition class is defined on the basis of an NUV–optical color cut; an a posteriori check of the 2dF spectra of these galaxies shows indeed that they have typically intermediate spectra between those of strongly star-forming and quenched galaxies.

The stacked spectra of the three spectral types are shown in Figure 4. Clearly visible is the transition from a spectrum dominated by stellar absorption for the quenched galaxies to a spectrum dominated by nebular lines for the strongly star-forming galaxies. The moderately star-forming galaxies present weaker emission lines than those observed in the strongly star-forming galaxies; as also highlighted below, they also have a redder continuum in comparison to the latter class. In Figure 4 we also indicate the median value of the 2dFGRS spectral parameter η for the three classes: in about 90% of the galaxies we find a good agreement between our classification and the one provided by the 2dFGRS team, with the remaining discrepancies due to spectral misidentifications, as discussed above.

5.2. Second Constraint to the Spectral Classification: FUV–NUV–optical Broadband Colors

The combination of FUV/NUV and optical/NIR colors has been shown to be a powerful tool to disentangle dust-reddened

⁹ These are the *eff-pop-syn-mid.dat* and *eff-telluric.dat* files, respectively. We did not attempt an absolute flux calibration of the spectra, which is beyond our purposes.

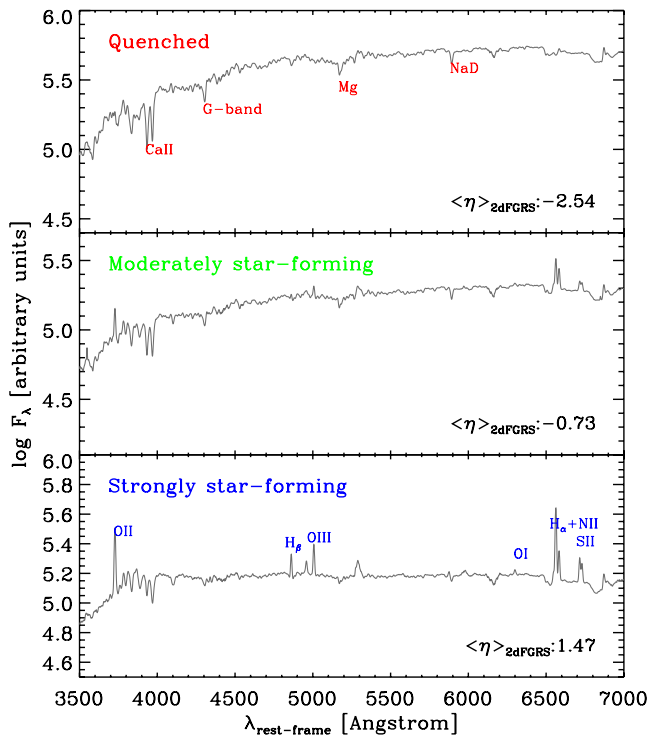


Figure 4. Stacked spectra of the ZENS galaxies classified as quenched, moderately star-forming, and strongly star-forming. The main emission/absorption features are indicated on top of the upper and lower panels. Quenched galaxies are characterized by strong stellar absorption lines and an underlying red continuum; star-forming galaxies have a blue continuum and intense nebular emission. The moderately star-forming type have properties that are intermediate between these previous two classes. Each composite spectrum is obtained from >300 individual spectra. The flux is given in logarithm of raw counts; hence, the absolute normalization is arbitrary. The median value of the spectral parameter η provided with the 2dFGRS database for the three spectral types is indicated on the bottom right of the panels. Note that in the original 2dFGRS classification scheme, quenched galaxies have $\eta < -1.4$, star-forming galaxies $\eta > -1.4$, and starbursts $\eta > 3.5$.

(A color version of this figure is available in the online journal.)

star-forming galaxies from red-and-dead quenched galaxies (Gil de Paz et al. 2007; Haines et al. 2008; Williams et al. 2009; Bundy et al. 2010). As an independent validation of the spectral classification of the ZENS galaxies presented above, we analyzed the two color–color diagrams illustrated in Figure 5, i.e., the $(\text{NUV} - I) - (B - I)$ and the $(\text{FUV} - \text{NUV}) - (\text{NUV} - B)$ diagrams. To this purpose we used the aperture photometry described in Section 3.1; rest-frame magnitudes were obtained using the k -corrections derived from the ZEBRA+ best-fit SEDs.

We used BC03 models to determine suitable color cuts in these diagrams for a three-bin spectral classification as discussed above. Specifically, the condition for galaxies to be classified as quenched was set to $\text{NUV} - I > 4.8$, $\text{NUV} - B > 3.5$, and $B - I > 1.2$; these color cuts identify >5 Gyr passively evolving SSP models (gray lines in the figure). Strongly star-forming galaxies were defined to have $\text{NUV} - I < 3.2$, $\text{NUV} - B < 2.3$, and $B - I < 1.0$, i.e., cuts that are consistent with the colors of 1–5 Gyr old stellar populations with a $\tau = 1$ Gyr exponentially declining SFH (black lines). Moderately star-forming galaxies are shown with green points in Figure 5 and were selected to have NUV–optical colors that fall between the two bracketing classes above.

The reddening arrow in the $(\text{NUV} - I) - (B - I)$ diagram moves galaxies parallel to the sequence defined in this diagram by the star-forming galaxies, but away from the region occupied by the

quenched galaxies. In contrast with the degeneracy observed for optical colors, the NUV–optical color–color diagram is thus particularly effective in discriminating dusty star-forming galaxies from quenched galaxies. Note that we do not use the FUV passband as a classification criterion, but its availability enables us to define an FUV–NUV color in the vertical axis of the right panel of Figure 5, which gives a further handle to verify the robustness of the different spectral types.

The filled symbols in Figure 5 show galaxies that satisfy both the spectral *and* color conditions that are required for qualifying as quenched and moderately/strongly star-forming galaxies. In the light of non-zero photometric errors, however, we expect that the sharp color cuts that we assumed introduce some degree of contamination from one to another of the different spectral classes. Most misclassifications are likely to show up as galaxies that do not satisfy simultaneously both spectral *and* color criteria qualifying a specific spectral class. Galaxies that did not satisfy simultaneously both classification criteria are shown as empty symbols in Figure 5; their spectra and images were visually inspected before they were finally assigned to a given spectral class. The categories of such objects are: (1) galaxies with a quenched spectrum but “blue” colors relative to normal quenched galaxies (there are 61 such galaxies in the entire ZENS sample); (2) galaxies with a strongly star-forming spectrum but with redder colors than normal star-forming galaxies; (3) a few galaxies, classified as moderately star-forming on the basis of their spectral features, that however do not satisfy simultaneously all $\text{NUV} - B$, $\text{NUV} - I$, and $B - I$ color selection criteria; and, finally, (4) a few (21) galaxies that nominally would fall in the “quenched” region of the color–color planes, but have clear emission in the H_α and are assigned to the moderately star-forming class.

Several factors contribute to category (1), i.e., to the detection of 61 absorption-spectrum galaxies with blue colors. About 40% of these systems are simply scattered in the NUV–optical color diagrams by photometric errors, and we assess that they are, at a visual inspection, rather normal quenched galaxies. In seven of these galaxies, instead, the analysis of the WFI B and I images shows that the fiber spectra catch mostly the light of a quenched bulge and leave low-level star formation in an outer disk undetected. For two other galaxies the spectra present line ratios that are indicative of AGN activity. In the remaining cases, however, the blue colors in these absorption-spectrum galaxies may interestingly indicate either a minor episode of star formation, which is causing the integrated color to become slightly bluer, or passively evolving populations that are on average younger than those of their redder counterpart. We thus further inspected the 2dFGRS spectra of these galaxies to search for possible “post-starbursts” features, specifically the presence of strong Balmer absorption lines (especially H_δ) but no significant [O II] emission (e.g., Dressler & Gunn 1983; Couch & Sharples 1987; Zabludoff et al. 1996; Poggianti et al. 1999, 2009). We adopted as the threshold for “strong” Balmer absorption an H_δ value equal to 1.5 times the median value of 1.67 Å measured for the sample of normal quenched galaxies. Twelve galaxies were found with such post-starburst spectra; these galaxies are accordingly flagged in the ZENS catalog published with Paper I. The reminder of the blue-but-quenched galaxies did not formally satisfy this quantitative criterion. They are also, however, flagged in the catalog, not as “post-starburst,” but as blue-but-quenched systems, to keep memory of their peculiarity. We postpone a detailed study of these galaxy populations to a future ZENS analysis.

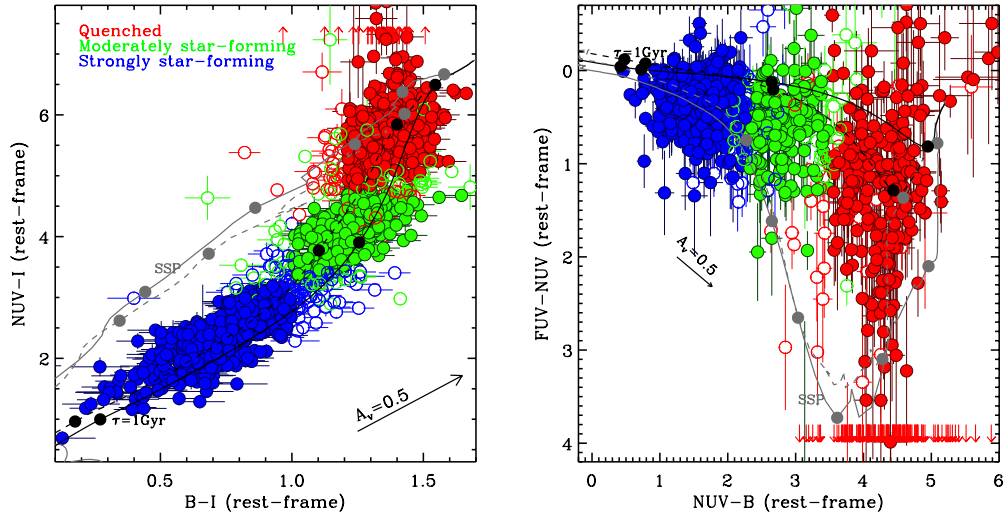


Figure 5. Color-color diagrams used, together with the original 2dF spectra, to classify ZENS galaxies in the three spectral types of strongly star-forming, moderately star-forming, and quenched galaxies. Left panel: rest-frame $(\text{NUV} - I)$ – $(B - I)$ color-color diagram. Quenched galaxies are shown in red circles, moderately star-forming galaxies in green, and strongly star-forming galaxies in blue. Filled points show galaxies that satisfy all color and spectral criteria used to define these classes; empty symbols are galaxies that do not meet some of the constraints but are assigned a given class after visual inspection of the spectral and imaging data. Red arrows show quenched galaxies that are undetected in the NUV; these are positioned at an arbitrary value along the vertical axis for visualization purposes. The lines are predictions for the color evolution of two synthetic models from the BC03 library, i.e., an SSP (gray) and an exponentially declining star formation history with an e -folding time of 1 Gyr (black lines), with a metallicity of $Z = Z_{\odot}$ (solid lines) and $Z = 0.4 Z_{\odot}$ (dashed lines). From left to right, the large black circles indicate the colors of these stellar populations at the ages of 0.5, 1, 5, and 10 Gyr. The effect of an $A_V = 0.5$ dust reddening vector is shown with an arrow. Conversion to rest-frame colors is obtained using the k -correction values given by the ZEBRA+ best-fit templates. Right panel: $(\text{FUV} - \text{NUV})$ – $(\text{NUV} - B)$ color-color diagram that we use to further check our spectral classification of ZENS galaxies. Symbols and lines are as in the left panel. Quenched galaxies that are undetected in the FUV are represented as arrows and are positioned at an arbitrary value along the vertical axis for visualization purposes.

We finally note that “red” galaxies with a star-forming spectrum (i.e., galaxies in category (2) above) are nevertheless generally bluer than the genuinely “quenched” galaxy population. Most of these red star-forming galaxies are disks with a relatively high inclination, i.e., ellipticity $\epsilon > 0.4$ (see Figure 6). The red colors of these objects are a consequence of dust obscuration.

Summarizing, the combination of the spectroscopic information discussed in the previous section with the (FUV and) NUV–optical photometric diagnostics discussed in this section leads to a robust spectral classification for the ZENS galaxies in the three classes of quenched, moderately star-forming and strongly star-forming galaxies. Note, however, that this classification does not provide a quantitative estimate for the SFRs of the galaxies, for which we rely on the ZEBRA+ SED fits. We therefore performed a further test of consistency between the galaxy spectroscopic classes (based on the analysis of spectral features and colors) and the SFRs (based on the ZEBRA+ SED fits), to ensure self-consistency between SFR estimates and spectral classification of the ZENS galaxy sample.

5.3. Quantitative SFRs from ZEBRA+ SED Fits

The top panel of Figure 7 shows the relation between sSFR and galaxy stellar mass M_{galaxy} , with highlighted in red, green, and blue the three spectral classes discussed above (color coding as in Figure 5). Not surprisingly and reassuringly, there is a very good agreement between the quantitative SED-based SFR estimates and the assigned spectral types. Galaxies classified as quenched based on their absorption spectral features and/or red NUV–optical colors have generally $\log(\text{sSFR}/\text{yr}) \lesssim -11$, i.e., at their current SFRs, it would take more than 10 times the present age of the universe (t_U) to double their mass. Strongly star-forming galaxies have $\log(\text{sSFR}/\text{yr}) \gtrsim -10$, i.e., mass-doubling times much shorter than t_U ; moderately star-forming galaxies fall in between the two bracketing classes. It should be

noted that the sample in Figure 7 includes quenched galaxies and is not complete in stellar mass at the low end, and so the steep slope of the sSFR–mass relation indicated in the figure should not be taken to indicate a highly negative value of β in the relation $\text{sSFR} \propto M^{\beta}$ (cf. Peng et al. 2010).

We highlight that in the ZENS sample there are 31 galaxies that are classified as moderately or strongly star-forming systems based on their spectral features and/or colors, but whose initial, unconstrained ZEBRA+ best fits resulted in incorrectly low sSFRs ($\log(\text{sSFR}) < -11.8$). We explored the origin of this inconsistency. For 17 of these “problematic” galaxies no *GALEX* photometry is available, and thus for them a reduced number of passbands were used to perform the SED fits, which are unconstrained at UV wavelengths. All but two of the remaining galaxies were found to have high inclinations; thus, the too low sSFRs are likely the result of an underestimation of the amount of dust reddening in such galaxies (the typical reddening is $E(B - V) = 0.08$ in the unconstrained fits). For all these galaxies, we thus re-run our ZEBRA+ fits constraining the latter to a star-forming SED model, specifically by only using constantly star-forming templates (csf) or templates with an exponentially decreasing SFH with $\tau = 2, 4, 6, 8$ Gyr and ages between 0.4 and 4 Gyr. The same metallicity and reddening as in Table 2 were used for these “constrained” ZEBRA+ runs. This led to revised SFR, stellar mass, and sSFR estimates (magenta symbols in Figure 7) for these 31 galaxies, which are flagged in the ZENS catalog that we have published in Paper I. As expected, the revised stellar masses are slightly larger (on average by 0.2 dex) than the mass estimates providing the clearly incorrect (i.e., too low) sSFRs. The column in the ZENS catalog that is used as a flag to identify these galaxies lists the “incorrect” galaxy stellar mass values for these 31 galaxies (and a dummy entrance for the remaining ones); the columns listing SFRs and sSFRs incorporate the “correct” values, obtained with the star-forming SED templates of the constrained ZEBRA+ fits. When

Table 3

Morphological Mix for the Three Spectral Classes in the ZENS Sample

Morphological Type	Quenched (%)	Moderately SF (%)	Strongly SF (%)
Ellipticals	100
S0s	91	7	1
Bulge-dominated spirals	67	22	11
Intermediate-type disks	44	29	27
Late-type disks	3	25	72
Irregulars	3	3	94

Note. For each of the morphological types of Paper II, the table lists the corresponding fractions for the different spectral types discussed in Section 5.

appropriate, we will test our analysis excluding these galaxies from our sample. We also, however, warn against a blind use of SED-fit-based estimates of SFRs and stellar masses, without suitable checks that these agree with the global colors and/or spectra of individual galaxies.

5.4. Spectral Types versus Morphological Types

We used the morphological classes determined in Paper II to examine the morphological mix within each of the spectral types defined above. These morphological mixes are listed in Table 3 and shown in the middle panel of Figure 7, which again plots the sSFR–mass relation as before, with highlighted in different symbols galaxies of the various morphological classes (with colors still representing the spectral type as before). As expected, there is a broad correlation between morphological and spectral types, i.e., E/S0 galaxies are largely quenched, and morphologically classified late-type disks are mostly strongly star-forming galaxies. Intermediate-type disks distribute themselves almost equally in the three spectral classes, and a third of the bulge-dominated spiral galaxies show some star formation activity. In Paper IV (C. M. Carollo et al., in preparation) we discuss in detail the morphological properties of quenched galaxies and the dependence of the quenched fraction on the different environments that we study in ZENS.

5.5. An Important Truism: Red Galaxies Are Not All Quenched Galaxies

Finally, the bottom panel of Figure 7 explicitly shows that, although quenched galaxies segregate into a tight optical “red sequence,” defined by our color cut $(B - I) > 1.2$, and moderately and strongly star-forming galaxies are respectively mostly located in “green-valley” and “blue-cloud” regions, both star-forming classes have $(B - I)$ colors that overlap with the red sequence of quenched galaxies.

This is further illustrated in the left panel of Figure 8, which shows the sSFR versus integrated $(B - I)$ color, and, explicitly, in the right panel of the same figure, which quantifies the contamination of star-forming galaxies to the “red sequence,” as defined through a simple optical color, in our case the $(B - I)$ color. Specifically, the right panel of Figure 8 shows, as a function of stellar mass, the fraction of galaxies that are classified as either strongly star-forming or moderately star-forming and have colors $(B - I) > 1.2$ (normalized to the total number of galaxies with such $(B - I)$ colors). We note that the relative importance of dust-reddened galaxies increases with decreasing stellar mass; at our completeness mass limit for quenched galaxies of $10^{10} M_{\odot}$ star-forming galaxies contribute up to $\sim 50\%$ of the nominal $(B - I)$ red sequence (assuming

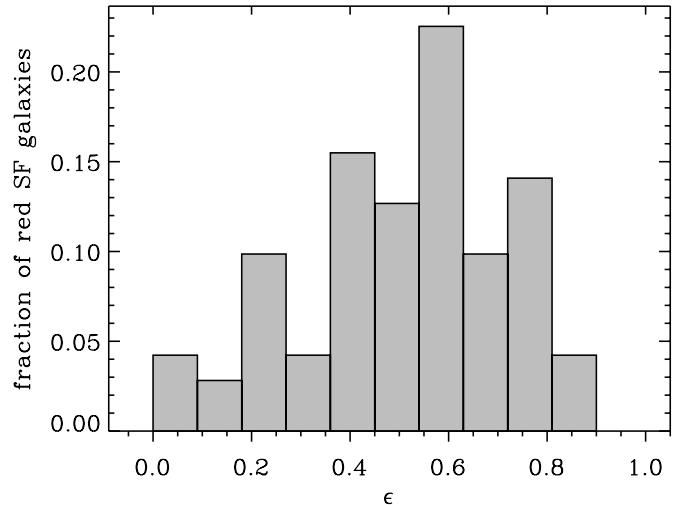


Figure 6. Distribution of ellipticities for galaxies that are classified as strongly star-forming based on the 2dF spectra, but which have red optical or NUV–optical colors. The majority of these galaxies have large ellipticities; also at a visual inspection, they are disk galaxies with large inclination angles. Thus, we attribute the reddening of their colors to dust obscuration.

that the reddening is in all cases attributable to dust effects only; a population with relatively low sSFR with respect to those expected for a given stellar mass may also be present within the *star-forming* class). This result is supported by independent analyses at similar mass scales (e.g., Bell et al. 2004; Davoodi et al. 2006; Haines et al. 2008; Maller et al. 2009).

6. $(B - I)$ TWO-DIMENSIONAL COLOR MAPS AND RADIAL COLOR GRADIENTS

To study the variation of stellar populations and distribution of star-forming regions within galaxies, we used the WFI B and I images to construct a two-dimensional $(B - I)$ color map for each galaxy. Since the B and I filter observations have different PSFs, we cross-convolved each passband with the PSF of the other passband. To prevent spurious color gradients arising from errors on the registration of the two images, we rebinned the original pixels in 7×7 sub-pixels before performing the registration of the B and I images using the IRAF task `imalign`. A correction for Galactic dust extinction was applied to the color maps.

6.1. Voronoi Tessellation

It is customary to perform a binning or smoothing of the spatial elements in astronomical images in order to homogenize the signal-to-noise ratio (S/N) across the sources (e.g., Sanders & Fabian 2001; Cappellari & Copin 2003; Ebeling et al. 2006; Zibetti et al. 2009). To increase the S/N of the ZENS WFI color maps in the outer regions of galaxies, where the flux from the sky background is dominant, we performed an adaptive local binning of pixels using a *Voronoi tessellation* (VT) approach.

The idea behind the method is to group adjacent pixels into bigger units that have a minimum scatter around a desired S/N (*uniformity requirement*). The tessellation should further satisfy a *topological* and *morphological* requirement, i.e., create a partition without gaps or overlapping regions, and a maximum roundness of the bins should also be attained. In the VT technique a density distribution of the S/N over the area of the galaxy is defined, $\rho(r) = (S/N)^2(r)$, and binning to a constant S/N is then ensured by determining regions of equal mass

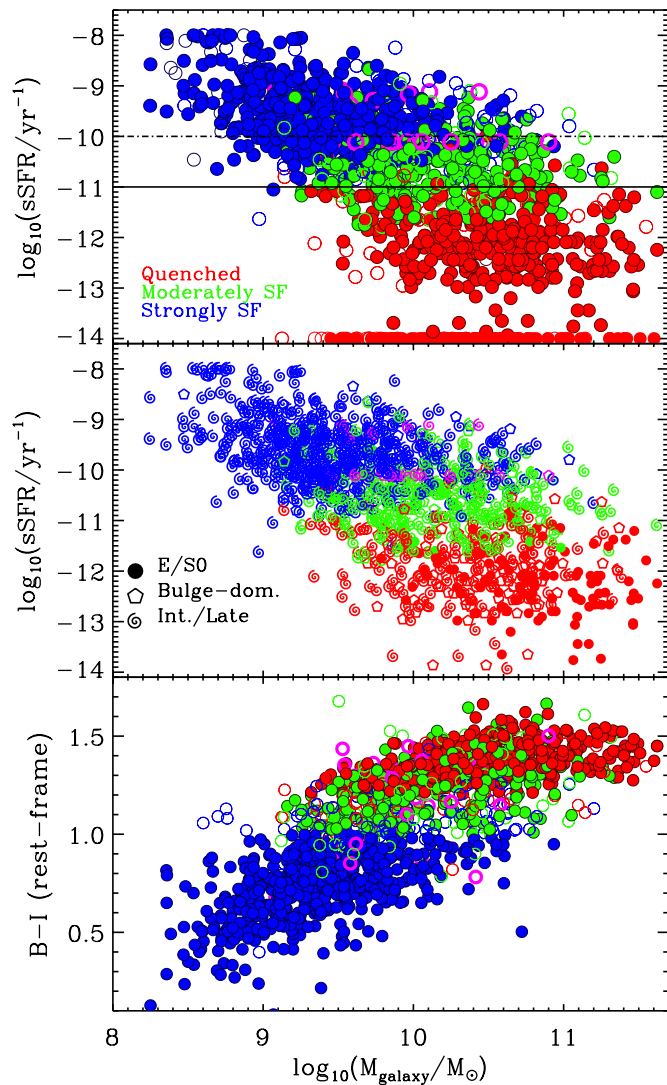


Figure 7. Top: location of the three spectral types on the sSFR vs. galaxy stellar mass relation. Symbols and colors are as in Figure 5. The horizontal dashed and solid lines mark the inverse of the current age of the universe and 10 times the current age of the universe, respectively. The 31 galaxies with “enforced” star-forming SED templates discussed in the text are identified with magenta (empty) symbols. Galaxies plotted at a constant $\log_{10}(\text{sSFR}/\text{yr}) = -14$ are quenched systems for which the best-fit SED model resulted in very low star formation rates ($\text{SFR} < 10^{-4} M_{\odot} \text{yr}^{-1}$). Middle: symbols in this panel correspond to different morphological types: ellipticals and S0s are shown with circles, pentagons are for bulge-dominated spiral galaxies, and intermediate-/late-type disks are shown with spiral symbols; colors are as before. Bottom: $(B - I)$ color vs. galaxy stellar mass. Symbols and colors are as in the top panel of the figure.

according to ρ . The VT method is often used to maximize the reliability of astrophysical information from noisy data (albeit at the expense of angular resolution; see, e.g., Ferreras et al. 2005; Daigle et al. 2006).

To perform the VT on the $(B - I)$ color maps of the ZENS galaxies, we used the publicly available IDL codes of Cappellari & Copin (2003),¹⁰ and in particular we adopted the generalization (*weighted voronoi tessellation*, *WVT*) proposed by Diehl & Statler (2006). For the code to work, along with the color map it is necessary to provide an estimate of the S/N of each pixel. We computed the error on each pixel using the cross-convolved images as $\sigma = 1.0857(\sigma_{\text{flux}}/\langle I \rangle)$. Here

$\langle I \rangle$ is the intensity in counts measured from the source. The flux error is the sum of Poisson fluctuations in the number of photons from the source plus random noise from the sky, i.e., $\sigma_{\text{flux}} = \sqrt{\langle I \rangle / g_{\text{eff}} + \sigma_{\text{sky}}^2}$, where g_{eff} is the effective gain of the image and σ_{sky} the standard deviation of the background; the use of the effective gain takes into account that Poisson statistics applies to the total number of electrons coming from the sources. Errors on the pixels of color maps were then obtained by adding in quadrature the errors in the two filters.

Pixels with very low S/N, which would affect the robustness of the algorithm, were excluded from the binning by imposing a minimum threshold of $\text{S/N}^2 = 0.05$, found to optimize the results. Pixels belonging to the background, defined as pixels at a distance > 1.5 Petrosian radii from the center of the galaxy, were also rejected by using a mask image. A target S/N of 10 was chosen to construct the binned color maps.

Figure 9 shows the comparison between the original, untessellated color maps and the VT maps, together with the azimuthally averaged S/N and color radial profiles derived from the original and tessellated images. The three galaxies in the figure are representative of the variety of observed color profiles: a galaxy with a negative or “normal” color gradient (redder center, bluer outskirts), a galaxy with a flat color profile, and a galaxy with a positive or “inverted” color gradient (bluer center, redder outskirts). The VT clearly enables a more robust measurement of the color distribution of galaxies at large radii and removes the high-frequency fluctuations associated with the noise in the original color maps, while retaining substantial information on lower frequency, physical color variations within galaxies.

6.2. Azimuthally Averaged Radial $(B - I)$ Color Profiles

Azimuthally averaged $(B - I)$ color profiles for the ZENS galaxies were obtained both from the tessellated color maps and from the GIM2D B - and I -band single-component Sérsic fit parameters derived and calibrated in Paper II (to which we refer for details of the fits and their calibration against residual PSF, ellipticity, and concentration biases). The advantage of the former approach is that color profiles from the color maps are a straight measurement from the data and are thus not affected by data-model mismatches; the advantage of the latter approach is the substantial removal of observational biases, including PSF smearing, which enables one in principle to study color profiles also within the PSF radius.

Logarithmic color gradients were in both cases calculated by fitting the linear relation $(B - I) = (B - I)_{r_{1/2}} + \alpha \log(r/r_{1/2})$ to the color radial profiles. The slope $\alpha = \Delta(B - I)/\Delta(\log r) \equiv \nabla(B - I)$ defines what we will refer to as the “radial color gradient”; $(B - I)_{r_{1/2}}$ defines the color at the galaxy half-light semi-major axis ($r_{1/2}$). These $(B - I)_{r_{1/2}}$ colors were converted from observed to rest frame using the k -correction derived from the ZEBRA+ fits.

Unless obvious, we will distinguish in the following and future papers between gradient parameters derived from the GIM2D analytic fits and those obtained from the VT color maps by adding the subscripts “GIM2D” and “Voronoi” to the symbols $\nabla(B - I)$ and $(B - I)_{r_{1/2}}$. Note that the agreement between the parameters of the color profiles obtained with the two approaches was found to be generally good; where systematic differences were identified, we studied the origin of such discrepancies and derived recipes to tie the two measurements to a common scale, as described in Section 6.2.1.

¹⁰ <http://www-astro.physics.ox.ac.uk/~mxc/idl/>

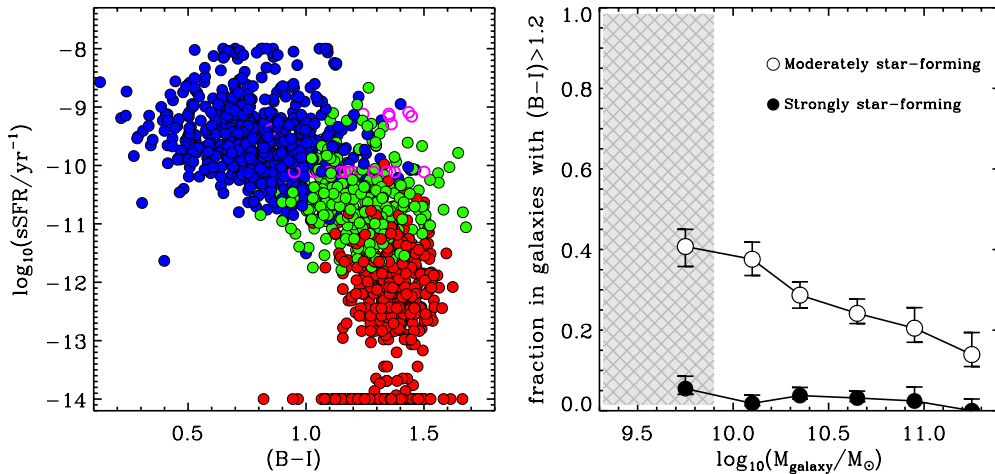


Figure 8. Left: sSFR as a function of galaxy integrated $(B - I)$ color. Symbols are color-coded according to the spectral type as in Figure 7 (galaxies plotted at a constant $\log_{10}(\text{sSFR}/\text{yr}) = -14$ are systems for which the best-fit SED model resulted in very low star formation rates, $\text{SFR} < 10^{-4} M_{\odot} \text{yr}^{-1}$). Right: fraction of galaxies with $(B - I) > 1.2$ (i.e., contaminants to the “optical red sequence” of quenched galaxies) that are classified as strongly star-forming (filled symbols) or moderately star-forming (empty symbols). The gray shaded area shows the region of mass incompleteness for quenched galaxies in the ZENS sample.

We adopt as our fiducial measurements in our future ZENS analyses the radial color profiles $\nabla(B - I)_{\text{GIM2D}}$ based on the analytical Sérsic fits; these fits were performed within the radial range $0.1r_{1/2} - 2.5r_{1/2}$. We will use, however, the parameters $\nabla(B - I)_{\text{Voronoi}}$ and $(B - I)_{r_{1/2}, \text{Voronoi}}$ derived from the VT color maps for the $\sim 5\%$ of ZENS galaxies for which no analytical fit could be derived, and also as a check of the analytical color profiles at relatively large radii ($> \text{FWHM}_{\text{PSF}}$).

The empirical Voronoi radial color profiles are affected by observational biases and require therefore some corrections. We detail below the main issues involving these estimates for the radial color profiles and the approaches that we have taken to minimize spurious observational effects in their estimates.

Finally, we note that the VT color maps contain more information than one-dimensional gradients; in particular, they enable us to study also the color rms dispersion (scatter) around the smooth average color profiles within galaxies. This was defined and computed as $\sigma(B - I) = \sqrt{\sum_i \xi_i^2 / N}$, with ξ residuals with respect to the azimuthally smoothed radial color profile.

In the last part of this paper we present a quick look into the colors, color gradients, and color scatter properties of disk satellite galaxies of all bulge-to-disk ratios in different environments.

6.2.1. Color Profiles and Color Scatter from the VT Color Maps: Corrections for Systematic Effects

Fits to the color profiles based on the VT color maps were limited between $r_{\text{PSF}} < r < r_{\text{MAX}}$, with r_{MAX} either $2.5 \times r_{1/2}$ for sufficiently high S/N maps, or the maximum radius over which the tessellation could be performed. The inner profile within the radius r_{PSF} , equal to the largest between the B and I seeing FWHM, was masked out to minimize the effects of PSF blurring. We assumed that, on large scales, the radial distribution of color in the galaxies is axisymmetric and joined together all the Voronoi bins that are crossed by the same ellipse of given semi-major axis when deriving the color profiles. To compute color gradients using the Voronoi maps, we masked out all Voronoi cells with colors $> 5\sigma$ away from a bi-weighted mean of the colors of all cells, or $> 3.5\sigma$ away from the best-fit linear regression to all cell colors as a function of radius. We checked that

these masking criteria exclude very bright compact star-forming regions/clusters and residuals from not perfectly cleaned nearby companions, without eliminating broader-scale fluctuations associated with internal variations in star formation activity. Radial color gradients $\nabla(B - I)_{\text{Voronoi}}$ and $(B - I)_{r_{1/2}, \text{Voronoi}}$ colors were then calculated with a Levenberg–Marquardt least-squares fit to the remaining Voronoi cell data.

As anticipated, the VT-based radial color gradients require some corrections. Not least, galaxy-to-galaxy variations prevent a homogeneous radial sampling of the color gradients among the entire sample: the minimum radius that is probed depends on the seeing under which a given galaxy was observed, and the maximum radius is often set by the noise of the image and the galaxy brightness and intrinsic size. Figure 10 shows the distribution of these minimum and maximum radii employed in the calculation of the color gradients from the Voronoi maps, in units of the galaxies, half-light radii. Rather comforting is that, for most of the sample, the fitted region spans a range of radii from well below $r_{1/2}$ up to $\sim 2.5 \times r_{1/2}$; in only 8% and 4% of the galaxies is the minimum radius larger than $0.7r_{1/2}$ and the maximum radius smaller than $1.3r_{1/2}$, respectively. Note that as shown on the inset in Figure 10, these two troublesome situations, however, never occur at the same time.

Also, PSF blurring and consequent masking of the central galactic regions (by one PSF’s FWHM) remain a source of concern for the reliability and stability of the derived $\nabla(B - I)_{\text{Voronoi}}$ values. In Figure 11 we plot the gradients $\nabla(B - I)_{\text{Voronoi}}$ as a function of r_{PSF} , in units of the galaxies, half-light radii. There is a correlation between the measured gradients $\nabla(B - I)_{\text{Voronoi}}$ and $r_{\text{PSF}}/r_{1/2}$: not surprisingly, the gradients become flatter with increasing FWHM of the PSF. To minimize this effect, at least in a statistical manner, we derived an empirical correction function by fitting a linear relation to the $\nabla(B - I)$ versus $r_{\text{PSF}}/r_{1/2}$ relation, which is shown with a dashed line in Figure 11. This empirical correction was then applied to all the Voronoi gradients.

Figures 12 and 13 show respectively the comparison between the corrected $\nabla(B - I)_{\text{Voronoi}}$ color gradients and the $(B - I)_{r_{1/2}, \text{Voronoi}}$ colors with the corresponding GIM2D measurements. For reference, we also show as black points the uncorrected Voronoi gradients in the last panel of Figure 12. Overall the two methods give qualitatively consistent results, particularly for the

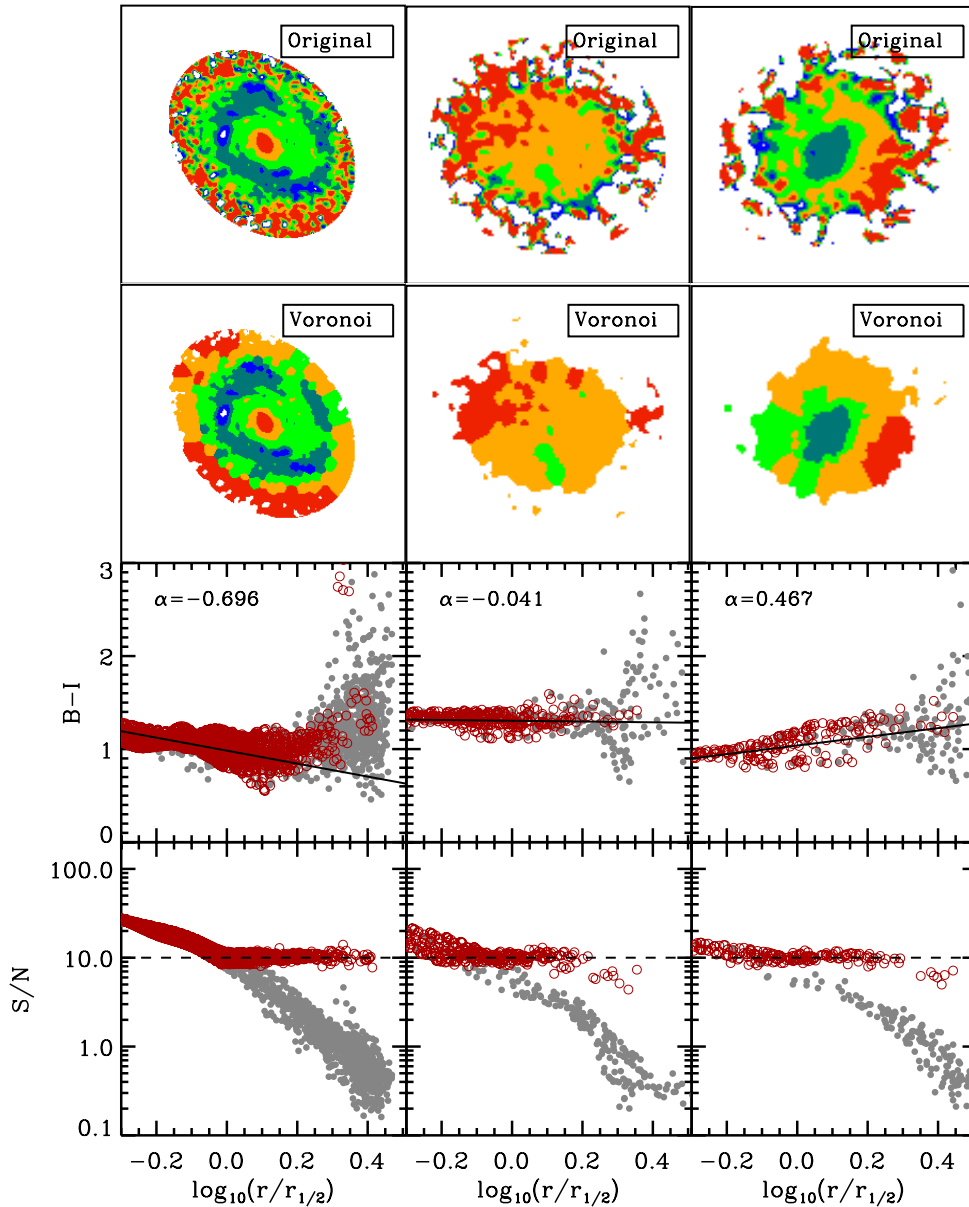


Figure 9. Examples of the Voronoi-tessellated color maps for three of the ZENS galaxies. From left to right the figure shows a galaxy with negative color gradient (i.e., outer regions bluer than the nucleus), one with a flat profile, and one with positive gradient (outskirts redder than the nucleus). The top panels show the original un-tessellated color maps; the second row from the top shows the Voronoi-tessellated maps. The next two rows are respectively the azimuthally averaged color and signal-to-noise radial profiles. Gray symbols correspond to the profiles derived from the original color maps (1 in 20 points plotted for clarity); black empty points (red in the online version) are the values obtained from the tessellated color maps. The lines in the third row panels are the best-fit linear relations to the tessellated profiles; the dashed lines in the bottom panels show the target S/N used for the tessellation. Radii are normalized to the galaxy half-light radius.

(A color version of this figure is available in the online journal.)

$(B - I)_{r_{1/2}}$ values. Concerning the color gradients, the above correction ameliorates the situation, but the Voronoi-based gradients tend to remain slightly shallower than the GIM2D-based gradients. To understand the origin of such residual difference, we searched for potential systematic biases with galaxy inclination, magnitude, minimum radius used in the fits, and size of the PSF.

There is indeed a bias with galaxy inclination: galaxies with $\epsilon > 0.6$ lie systematically below the identity line in the first panel of Figure 12, mostly as a consequence of projection effects. Along the semi-minor axis, where projection effects are strongest, for example, a given Voronoi cell integrates a larger range of physical radii, causing color information to be smeared out and color profiles to be slightly flattened at these high inclinations. The difference between the Voronoi and

GIM2D profiles depends also on galaxy magnitude: the difference is larger for fainter ($I > 17.5$) galaxies, whose $\nabla(B - I)_{\text{Voronoi}}$ and $(B - I)_{r_{1/2}, \text{Voronoi}}$ are respectively flatter and ~ 0.1 mag redder than the corresponding GIM2D measurements. This is most likely due to the contribution from the night sky noise, which becomes more significant at the low surface brightness regime and longer wavelengths. After the application of the correction delineated above, no strong biases were however observed with the absolute or relative size of the PSF in either the Voronoi gradients or the Voronoi $(B - I)_{r_{1/2}}$ colors.

Given the above, and in order to recover measurements of color gradients and colors at the half-light radius for galaxies without GIM2D fits (and minimize the bias in these measurements), we calculated the median residual differences between Voronoi and GIM2D color gradients and colors at the half-light

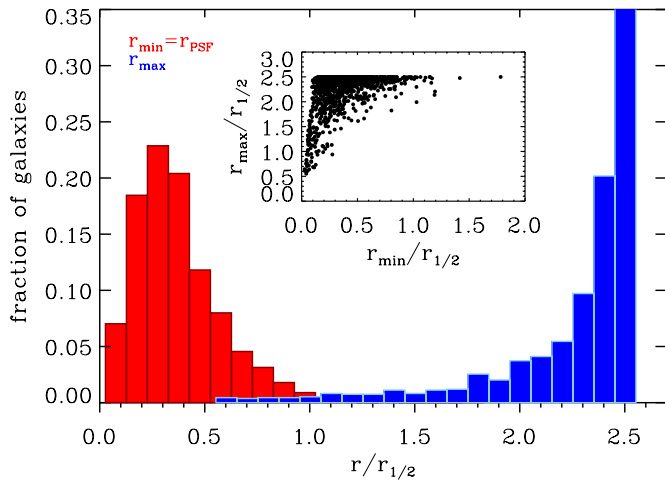


Figure 10. Distribution of minimum and maximum radii, in units of the global galaxy half-light radius, used to fit the azimuthally averaged color profiles derived from the Voronoi-tessellated color maps. The minimum radius r_{PSF} is defined as the maximum between the B - and I -band PSF size. The inset shows the comparison between the minimum and maximum radius used for each galaxy (in units of the galaxy half-light radius).

(A color version of this figure is available in the online journal.)

radii, as a function of galaxy inclination and magnitude, and applied these additional correction functions to those galaxies for which no analytic color profile is available.

We finally highlight that, since (1) color gradients of highly inclined (disk) galaxies as well as marginally resolved galaxies ($r_{1/2} < 1.5 \times \text{PSF}$) are, even when using GIM2D estimates, subject to larger errors, and (2) high inclinations and small sizes may exacerbate physical biases introduced by absorption of light by interstellar dust, in our ZENS analyses, including those discussed in the following sections of this paper, we check that results hold when such galaxies are excluded from the sample. Similarly, we also check that results also hold when excluding galaxies with no GIM2D fits, i.e., galaxies for which we use the Voronoi gradients and colors (calibrated as above) in our analyses.

7. VARIATIONS IN MEDIAN SATELLITE/CENTRAL GALAXY STELLAR MASS ACROSS ENVIRONMENTAL BINS

Given (1) the main goal of ZENS, i.e., to study differential behaviors in similar galaxy populations as a function of several environmental diagnostics, and (2) the known sensitivity of galaxy properties to galaxy stellar mass, it is essential to keep under control, in any given galaxy sample, possible variations of galaxy mass distributions in the different environmental bins, as any such variation may induce spurious environmental effects. Consequently, before proceeding with our environmental analyses, we investigated whether the stellar mass distributions of ZENS galaxies of different morphological or spectral types vary with the environmental diagnostics derived in Paper I.

Figure 14 plots, from top to bottom, the median galaxy mass of the various morphological and spectral types as a function of group mass M_{GROUP} , distance from the group center (in units of R_{200}), and large-scale overdensity δ_{LSS} , considering only galaxies above the completeness limit of each type (i.e., the mass complete samples that will be used in our ZENS analyses). We initially include *all* galaxies of a given type in this analysis, independent of whether they are central or satellite galaxies. Overplotted in Figure 14, with thick lines in matching colors for

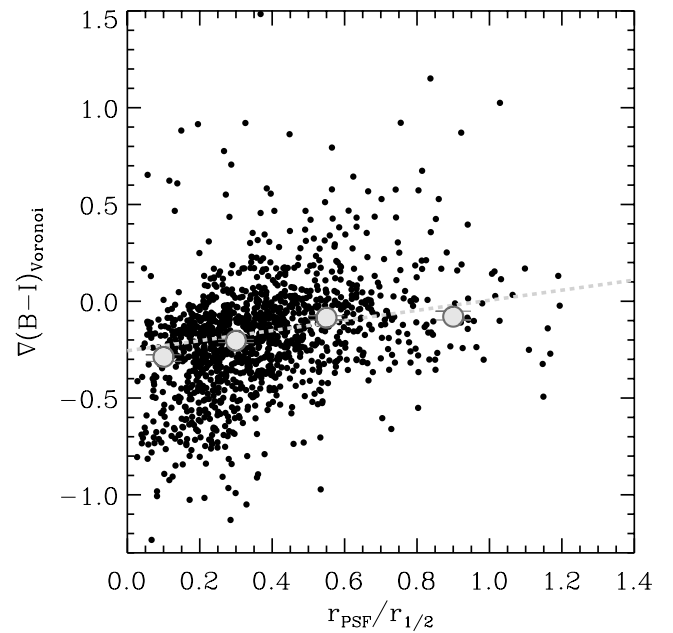


Figure 11. Color gradients $\nabla(B-I)_{\text{Voronoi}}$, i.e., derived by fitting the azimuthally averaged color profiles obtained from the Voronoi-tessellated color maps as a function of the minimum radius used in the fits (in units of the half-light radius). Large gray points indicate the average color gradient in four bins of $r_{\text{PSF}}/r_{1/2}$; the dashed line is the result of the 3σ -clipped linear least-squares fit used to statistically correct the raw $\nabla(B-I)_{\text{Voronoi}}$ values.

the various galaxy samples, are the median galaxy masses of the various morphological and spectral types for the corresponding *satellite-only* samples. The behavior of central galaxies can be inferred by comparing those of total and satellite-only samples.

The median masses of the different morphological and spectral types for all galaxies are sufficiently constant over the three environments to be confident that our analyses, at a *fixed* galaxy type, will not be biased by strong trends between galaxy stellar mass and any of the ZENS environmental parameters. Small variations of galaxy stellar mass with the environments are present for some of the galaxy populations: there is a modest ~ 0.1 dex increase in the stellar mass of moderately and strongly star-forming galaxies with increasing group mass from $\sim 10^{12.5} M_{\odot}$ to $M \gtrsim 10^{14} M_{\odot}$; for these spectral types, a similar mass trend is observed with increasing LSS (over)density.

For morphologically split galaxy samples including centrals plus satellites, the intermediate-type disks show a dependence with M_{GROUP} increasing their mass by 0.2 from low- to high-mass groups. A variation of galaxy mass is also detected with δ_{LSS} for E/S0 galaxies, whose median mass is larger by 0.2 dex at high LSS densities relative to similar galaxies at low δ_{LSS} values. There is furthermore an increase of the typical stellar mass of all spectral and morphological types when moving closer to the group centers. The latter trend weakens, however, substantially when central galaxies are excluded, indicating that the effect is mostly due to the addition of the central galaxies and is largely absent from the satellite population (see also Biviano et al. 2002; Pracy et al. 2005; von der Linden et al. 2010). For the other two environments, the trends for satellite galaxies match quite reasonably those discussed above for all galaxies, independent of their satellite/central raking.

These results support a scenario in which galaxy stellar mass are, at fixed morphological or spectral type, largely insensitive to the environment, and especially to the halo mass. A constancy of the galaxy stellar mass of the different galaxy

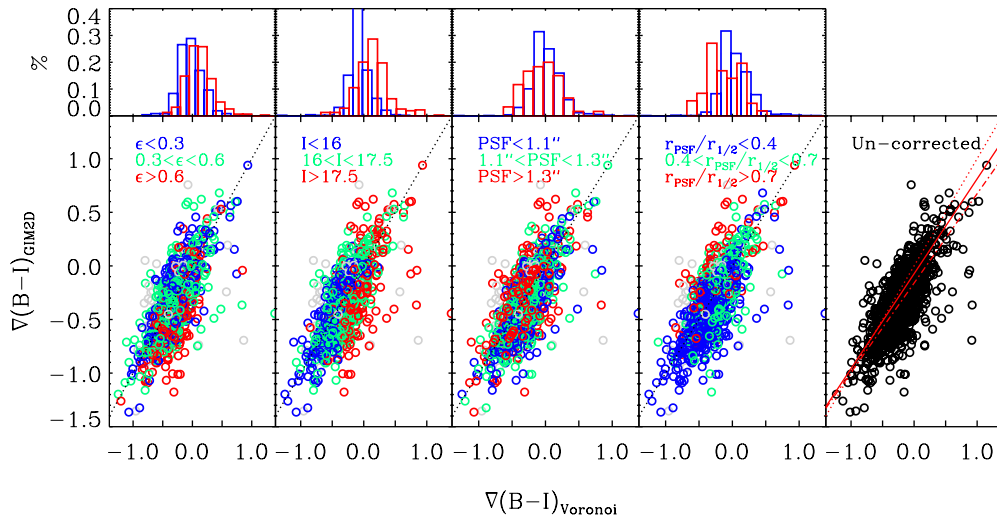


Figure 12. Comparison between color gradients $\nabla(B - I)_{\text{Voronoi}}$ derived from fits to the average color profiles obtained from the Voronoi-tessellated color maps and color gradients obtained from the analytical GIM2D Sérsic fits to the B - and I -band surface brightness profiles. ZENS galaxies are color-coded according to a number of observational diagnostics: from left to right, these are galaxy ellipticity, I -band magnitude, the maximum size between the B - and I -band PSF, and minimum radius used in the fits to the color profile. In the last panel the black points show the values of the Voronoi gradients before applying the empirical correction that takes into account the effect of masking the central r_{PSF} region. The histograms on top of each panel show the distributions of differences between Voronoi and GIM2D gradients in the lowest (blue) and highest (red) bin of the given parameters. Dotted lines indicate the identity line. In the right-most panel, solid and dashed-dotted lines are the best fit to the corrected for central masking and uncorrected $\nabla(B - I)_{\text{Voronoi}}$ measurements. Gray symbols identify “troublesome” galaxies with possible bright star contamination to their photometry or whose fits to the color profiles are restricted within 1.3 half-light radii or less.

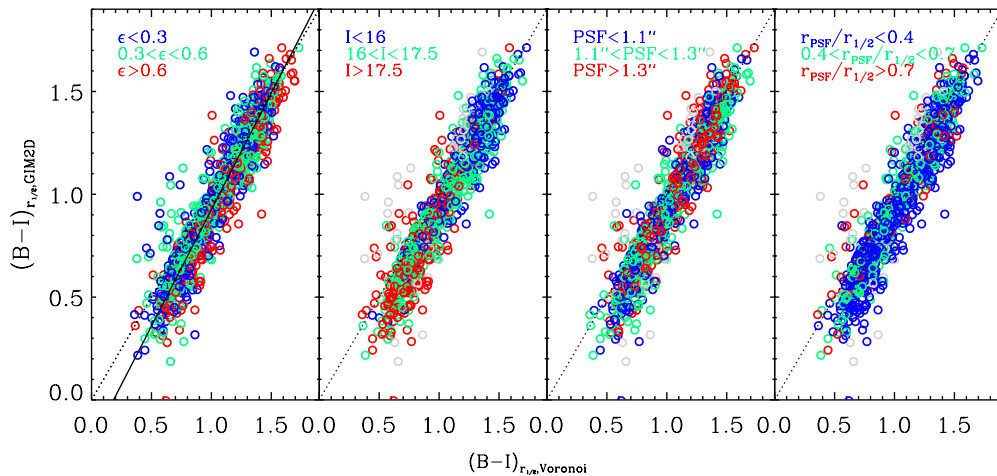


Figure 13. As in Figure 12, but for the $(B - I)_{r_{1/2}}$ measurements. The dotted and solid lines show the identity line and the fit to the points, respectively.

types with environmental density has been reported by a number of authors. The morphologically split galaxy mass functions for the COSMOS field given by Pannella et al. (2009) show consistency in over- and underdense regions. Bolzonella et al. (2010) and Kovač et al. (2010), using the zCOSMOS survey data (Lilly et al. 2007, 2009), find remarkably similar mass functions for morphological and spectral early- and late-type galaxies, across the lowest and highest density quartiles up to redshifts of order $z \sim 1$. Analogous results are obtained by Peng et al. (2010) on the local SDSS sample of blue galaxies. In the Peng et al. (2010) formalism, mass quenching is the only mass-dependent quenching term (environment quenching is independent of stellar mass), and it is therefore this process that establishes and controls the mass function of the surviving star-forming galaxies, and therefore also of the resulting passive galaxies. The observed constancy of the characteristic M_* with redshift, back to $z \sim 3$ or higher, sets the required form of mass quenching. Furthermore, as discussed in Peng et al. (2012), the fact that satellites (over a wide range of halo mass) and

central galaxies have globally a very similar M_* indicates that mass quenching operates in a very similar way in centrals and satellites.

Note that some contrasting evidence has been reported. The mass function of star-forming galaxies measured by Giodini et al. (2012), for example, has an identical shape in the field and in a sample of X-ray-selected groups, but shows a mild increase of the characteristic M_* mass in low-mass groups with respect to more massive systems. Calvi et al. (2012) also report a change in the morphology–mass relation for binary systems, clusters, and field galaxies.

This concludes our detailed presentation of the derivation of the photometric diagnostics for the ZENS galaxies. The measurements presented in the sections above will be used in future ZENS papers for detailed analyses of the stellar population and star formation properties of different galaxy populations as a function of different environmental parameters. In the remainder of this paper we present a first utilization of some of these measurements and briefly investigate (1) global

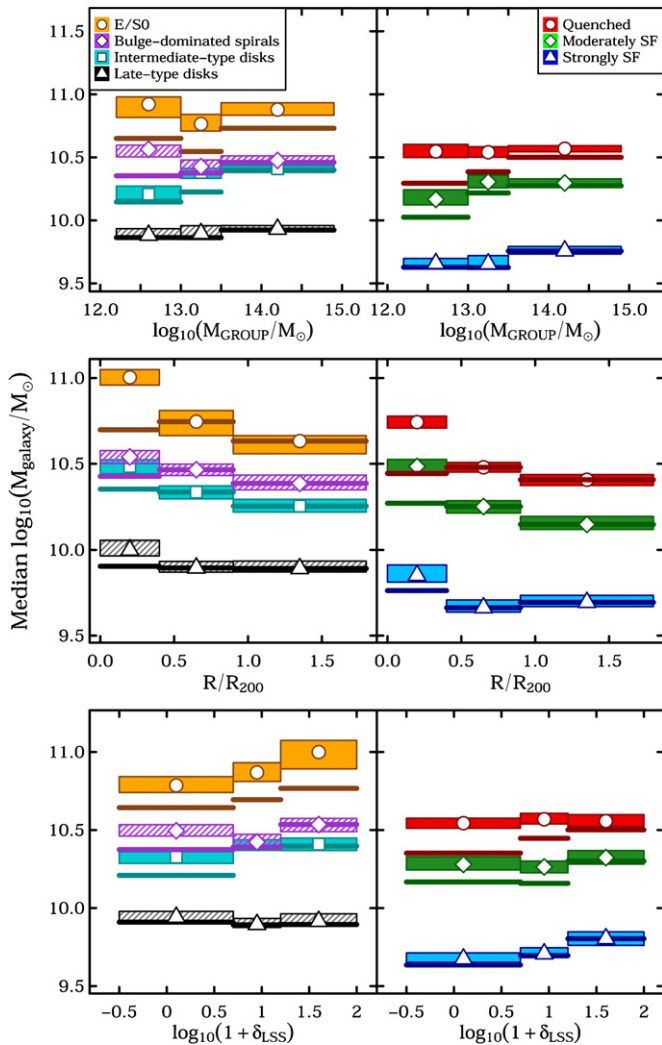


Figure 14. Median galaxy stellar mass as a function of environment for galaxies of different morphological (left) and spectral types (right; see legends for details). From top to bottom the considered environments are group halo mass, distance from the group center, and large-scale density. Median values are calculated above the mass completeness of each spectral/morphological type. Error bars, shown with hatched areas, represent the standard deviation of the median masses computed from the 16th and 84th percentiles. Colored boxes with white open symbols indicate samples including *all* galaxies, independent of their rank as centrals or satellites. The thick solid lines in matching colors are the results for *satellite-only* samples.

(A color version of this figure is available in the online journal.)

behavior of colors, color gradients, and color dispersions of all galaxies (i.e., centrals plus satellites) at fixed stellar mass and fixed Hubble type (from Paper II); and (2) colors, color gradients, and color dispersions of *disk satellites* in different environments.

8. COLORS, COLOR GRADIENTS, AND COLOR DISPERSIONS WITHIN GALAXIES: DEPENDENCE ON GALAXY STELLAR MASS AND HUBBLE TYPE

Figure 15 shows, from top to bottom, the median values of the $(B - I)_{r_{1/2}}$, $\nabla(B - I)$, and $\sigma(B - I)$ distributions as a function of galaxy stellar mass and at fixed Hubble type. We remind that we use the GIM2D-based estimates for $(B - I)_{r_{1/2}}$, $\nabla(B - I)$, and in the following drop the subscript “GIM2D” for simplicity of notation. The colors at the half-light radii show the expected trends: they get redder with increasing galaxy mass

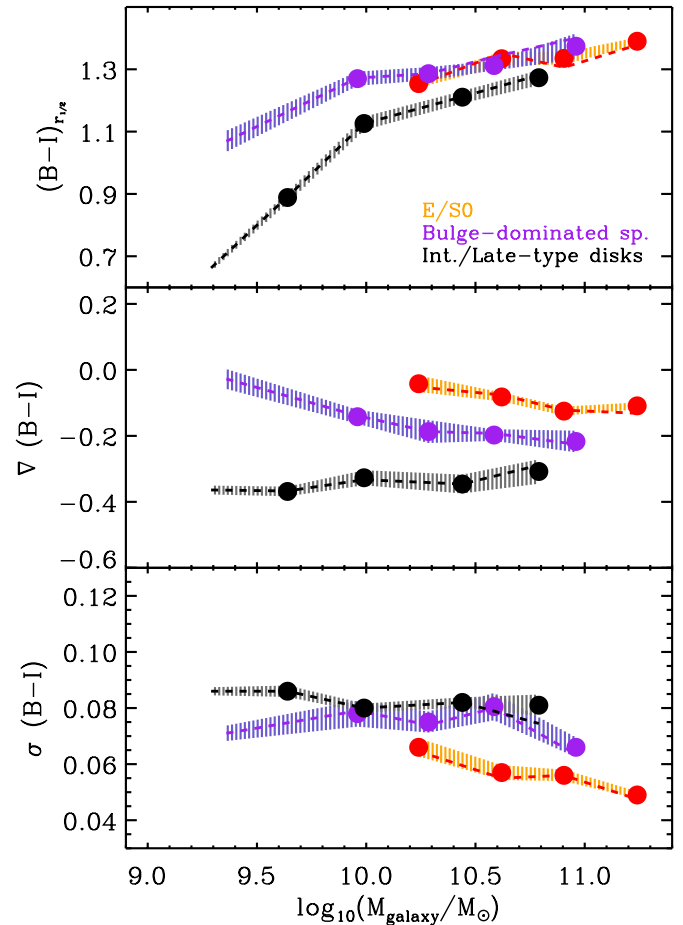


Figure 15. For the ZENS galaxies, from top to bottom, median colors at the half-light radii, color gradients, and rms scatter around the best-fit color profiles as a function of galaxy stellar mass. Colors correspond to the three morphological classes as identified in the legend (and defined in Paper II). The shaded areas with filled points show the median relations and the 1σ confidence levels for the entire ZENS sample with no distinction among centrals and satellites. The left-most filled symbol in each curve identifies the stellar mass completeness threshold for the given galaxy population. The dashed lines are for satellite galaxies only.

(A color version of this figure is available in the online journal.)

and progressively earlier Hubble types. Also not surprising is the strong dependence of the color gradients on the morphological type: E/S0 galaxies show the flattest profiles, an indication that these galaxies have rather homogeneous stellar populations from their inner to their outer regions; late(r) morphological types show stronger color gradients, mostly as a consequence of redder bulges and segregation of star-forming regions in the outer-disk regions.

Within each Hubble type, however, color gradients are rather insensitive to stellar mass variations and are typically $\nabla(B - I) \sim -0.3$ for intermediate- and late-type disks and $\nabla(B - I) \sim -0.1 / -0.2$ for earlier morphological types. Also the color dispersion around the average color profile, $\sigma(B - I)$, is largely independent of galaxy mass for intermediate-type and late-type disk galaxies. E/S0 galaxies instead show a net increase in color scatter around the average color gradient with decreasing galaxy stellar mass. We note that, in the mass bins $M \gtrsim 10^{10.5} M_{\odot}$, about half of the disk-dominated galaxies are also central galaxies in our sample. When the latter are excluded from the analysis, there is a hint (at the 2σ level between $\sim 10^{9.5} M_{\odot}$ and $M \gtrsim 10^{10.5} M_{\odot}$) for a modest decline in the color dispersion

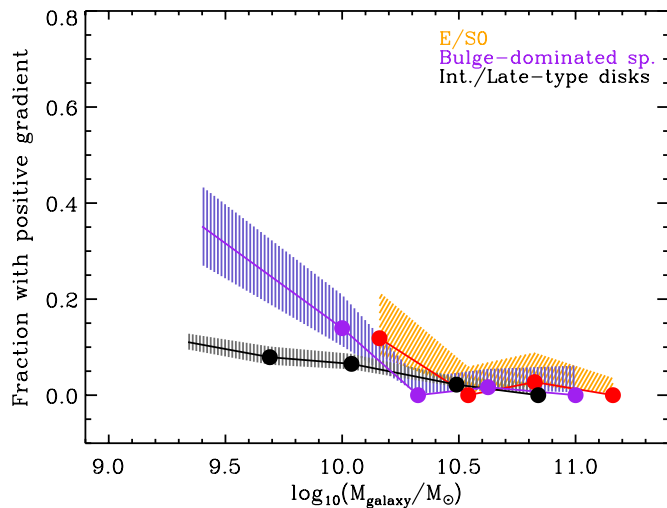


Figure 16. Fraction of galaxies with positive (“inverted”) color gradients, i.e., with blue nuclei and red outskirts, as a function of galaxy stellar mass at fixed morphological type. Shaded areas show the 1σ confidence levels on the fractions, derived using the beta distribution quantile technique (see Cameron 2011). The fractions are corrected for 2dFGRS spectroscopic incompleteness. The left-most filled symbol in each curve identifies the stellar mass completeness threshold for the given galaxy population.

(A color version of this figure is available in the online journal.)

with increasing galaxy stellar mass also in this morphological type; this is shown by the dashed lines in Figure 15. The inclusion of central galaxies has instead no significant impact for the earlier morphological types.

Also noticeable is that a non-negligible fraction of galaxies have positive color gradients, i.e., bluer centers relative to redder outer regions. Specifically, we divide the sample into three bins of color gradients, i.e., $\nabla(B - I) < -0.1$ (negative/normal color gradients), $-0.1 < \nabla(B - I) < 0.1$ (flat color gradients), and $\nabla(B - I) > 0.1$ (positive/inverted color gradients), respectively. Figure 16 shows the frequency of galaxies with positive gradient as a function of galaxy stellar mass, again at fixed morphological type as before. The fraction of galaxies with inverted color gradients increases with decreasing galaxy stellar mass: above $10^{10.5} M_{\odot}$ virtually no galaxies have inverted color gradients, while at $10^{9.5-10} M_{\odot}$ between 10% and 20% of galaxies have such inverted color profiles, with the higher fraction interestingly detected for earlier morphological types (in particular, bulge-dominated spirals, which are well sampled down to $\sim 10^{9.8} M_{\odot}$ in our sample).

We explore the spectral types of galaxies with $\nabla(B - I) > 0.1$, which are found at all group halo masses in the ZENS sample. In absolute terms the number of elliptical and S0 galaxies with inverted color profiles is negligible; thus, we focus in the following on the bulge-dominated spirals and intermediate/late-type disks; furthermore, as blue core galaxies are rare at high galaxy masses (see Figure 16), we consider only the $10^{9.5-10.5} M_{\odot}$ mass interval. We find that 70% of bulge-dominated spirals with inverted profiles are classified as either moderately or strongly star-forming (for a median specific star formation rate $\langle \log(\text{sSFR}/\text{yr}^{-1}) \rangle = -10.67$). While we should keep in mind the caveat that quenched and intermediate spectral type galaxies are somewhat incomplete in ZENS at masses $\lesssim 10^{10} M_{\odot}$, these values are meaningful in a relative sense, i.e., in comparison with galaxies of similar mass and morphological class and “normal” color gradients; these have a star-forming fraction of only 24% and $\langle \log(\text{sSFR}/\text{yr}^{-1}) \rangle = -12.22$. This

indicates an enhancement of SFR in bulge-dominated galaxies with blue cores. In contrast, late-type disks with $\nabla(B - I) > 0.1$ or $\nabla(B - I) < 0.1$ have overall similar star-forming fractions and SFRs. Other authors have already commented that tidal perturbations and/or ram-pressure removal of the outer gas reservoir in galaxies in groups may induce an enhancement of star formation in the galaxy cores (e.g., Koopmann & Kenney 1998; Moss & Whittle 2000; Bartholomew et al. 2001; Rose et al. 2001). We defer to a subsequent paper a more detailed investigation of these inverted-color-gradient galaxies, in particular in relation to internal color differences between satellite galaxies and between merging/interacting galaxies and their non-interacting counterparts.

9. COLORS, COLOR GRADIENTS, AND COLOR DISPERSION OF DISK SATELLITE GALAXIES IN DIFFERENT ENVIRONMENTS

We finally investigate, for the population of *disk satellite galaxies*, how the colors, color gradients, and color dispersion around these gradients depend, at constant stellar mass, on the total mass of the host group halo M_{GROUP} , the distance of the satellites from the centers of their host groups (R/R_{200}), and the large-scale (over)density field δ_{LSS} . In ZENS, disk morphologies account for 80% of the satellite population at $M < 10^{10} M_{\odot}$ and 53% at $M \geq 10^{10} M_{\odot}$, providing a statistical sample that is large enough for this straightforward environmental analysis over about 2 dex in stellar mass. We postpone to a follow-up ZENS study the comparative analysis of centrals and satellites, as well as the inclusion of elliptical and irregular morphologies, as both require a more elaborate discussion concerning biases toward one or another of these galaxy populations in both the stellar mass and halo mass ranges of our survey.

We first remark (without showing in a figure) that both bulge-dominated and disk-dominated satellites have *nuclear* $(B - I)$ colors, i.e., colors measured from the PSF-corrected profiles at $0.1r_{1/2}$, which are fairly insensitive to any of the environmental parameters: all disk satellite populations under investigation (i.e., different bulge-to-disk ratios and different galaxy stellar masses) have similar central colors, ranging from ~ 1.2 to ~ 1.4 , which become redder with increasing galaxy mass, but with environmental variations at constant mass that are smaller than ~ 0.05 mag.

In Figure 17 we show, from top to bottom, median values for the $(B - I)$ colors (integrated within the Petrosian aperture defined in Section 3.1), color gradients $\nabla(B - I)$, and color dispersions $\sigma(B - I)$, as a function of galaxy stellar mass for the satellite galaxies. Red is used for the broad morphological bin of *bulge-dominated* galaxies¹¹; blue indicates the broad morphological bin of *disk-dominated* galaxies.¹²

All median values were calculated in three bins of stellar mass using a box of width 0.4 dex for the disk-dominated galaxies and, considering the smaller size of the sample, in two mass bins below and above $10^{10.5} M_{\odot}$ for the bulge-dominated galaxies. In all bins in each panel, the used galaxy samples are above the mass completeness limits of the relevant morphological types, apart from a very marginal incompleteness in the lowest mass bin for the disk-dominated galaxies, as the intermediate-type

¹¹ The broad bin of bulge-dominated galaxies includes disk galaxies that are classified as S0 or bulge-dominated spirals in Paper II, to which we refer for details on the ZENS morphological classification.

¹² The broad bin of disk-dominated galaxies includes the two narrower morphological bins of intermediate-type and late-type disks defined in Paper II.

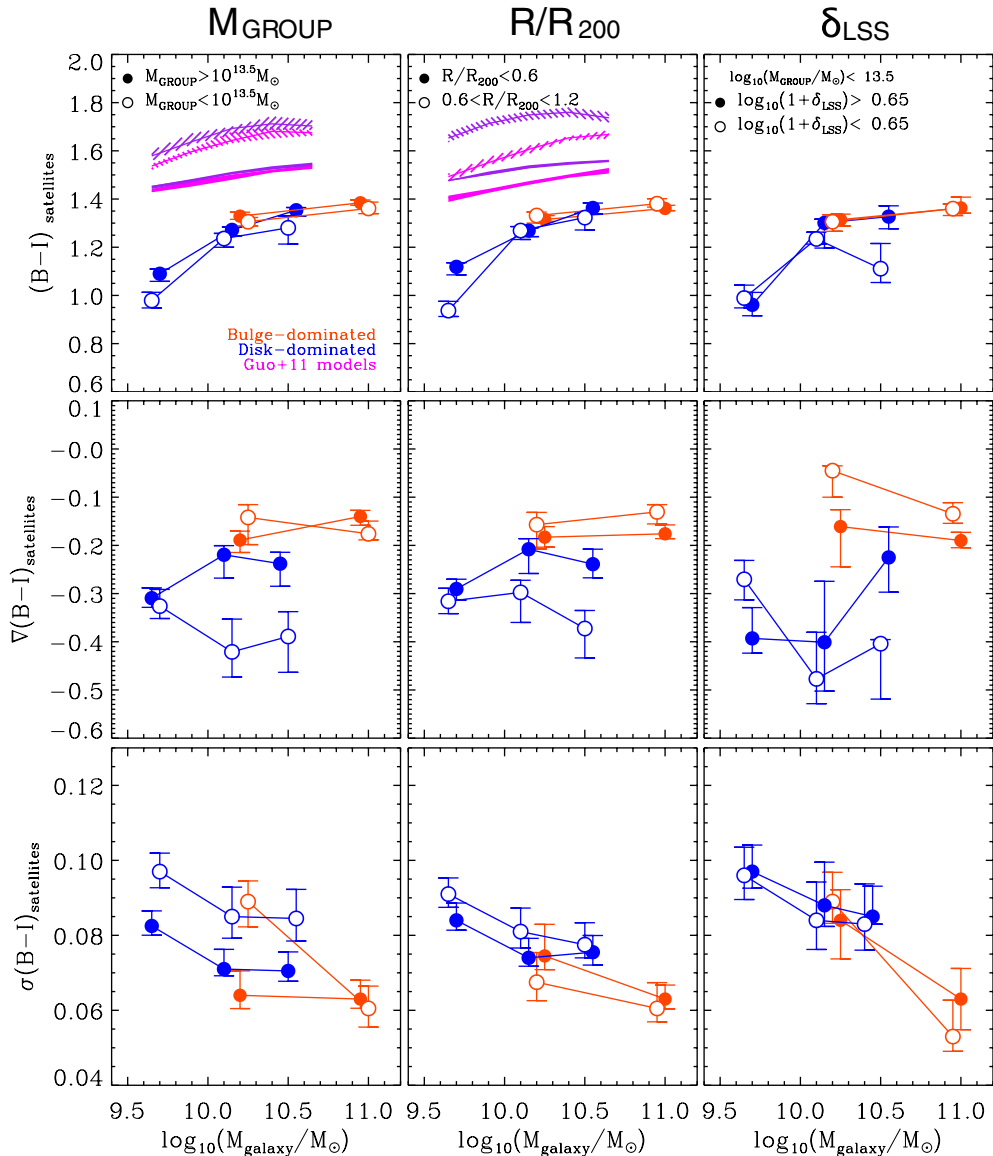


Figure 17. $(B - I)$ color (top panels), color gradients (central panels), and rms scatter around the best-fit color profiles (bottom panels) as a function of the galaxy mass for *disk satellites* in the ZENS groups. Red and blue identify respectively bulge-dominated satellites and disk-dominated satellites. From left to right, the galaxy sample is split into two environmental bins of group mass M_{GROUP} , group-centric distance R/R_{200} , and LSS overdensity δ_{LSS} , respectively. Error bars correspond to the error on the median derived from the 16th and 84th percentiles. In magenta and purple we show the predictions of the Guo et al. (2011) semi-analytical model for the sparser (low group mass and high group-centric distances) and denser (high group mass and low group-centric distances) environments, respectively; dashed and solid curves are for models with and without dust reddening. Strongly star-forming galaxies with red colors (i.e., dust-reddened galaxies; see Section 5.2 and Figure 5) are excluded from this analysis; the effects of their inclusion are in any case minimal. Trends with the δ_{LSS} field are investigated restricting the sample to groups with $M_{\text{GROUP}} < 10^{13.5} M_{\odot}$, to avoid spurious effects with increasing δ_{LSS} due to the degeneracy between high δ_{LSS} values and high group mass.

(A color version of this figure is available in the online journal.)

disks (which are summed together with the late-type disks to build this broader morphological late-type bin) are formally complete only above a slightly higher stellar mass bin; see Section 3.3. We checked, however, that this small effect does not impact our results, as also discussed below.

In Figure 17, filled and empty symbols show respectively “dense” and “sparse” environments, i.e., from left to right, group masses M_{GROUP} above and below $10^{13.5} M_{\odot}$ (left panels), group-centric distances larger and smaller than $R = 0.6R_{200}$ (central panels), and LSS overdensities above and below $\log_{10}(1 + \delta_{\text{LSS}}) = 0.65$, respectively. Note that the δ_{LSS} analysis includes only groups with $M_{\text{GROUP}} < 10^{13.5} M_{\odot}$, to minimize the degeneracy between group mass and LSS density: as discussed in Paper I, while by definition massive groups are located in

high- δ_{LSS} regions, low-mass groups cover a large range of LSS density regimes, thus enabling the disentanglement of effects due to one or the other of these two environmental parameters. All ZENS groups were otherwise used in this study, to increase the statistics, including the groups defined as unrelaxed in Paper I (see also Section 2); we checked that, with slightly larger error bars, consistent results hold when excluding the unrelaxed groups from the analysis. However, following the same approach as in Paper II, we limit the sample to galaxies with $R \leq 1.2R_{200}$ to minimize contamination from interlopers and/or small subhalos at large radii (see Paper I for a discussion).

For clarity, we split below the discussion on the environmental trends seen in Figure 17 separately for the bulge- and disk-dominated satellite populations.

9.1. Environmental Impact on Bulge-dominated Satellites

The most evident environmental effect we observe in Figure 17 for bulge-dominated satellites is the fact that they show systematically shallower color gradients at low (i.e., in the group outskirts and at low δ_{LSS}) relative to high environmental densities (i.e., inner-group regions and at high δ_{LSS}). This effect is seen in our data at a 3σ level in the bin at high galaxy stellar mass centered around $10^{11} M_{\odot}$ for δ_{LSS} . As indeed evident from Figure 17, however, the significance of the effect depends, for each environment, on the specific galaxy mass scale and, in some of the mass bins, it goes down to the $\lesssim 2\sigma$ level; still, its systematic nature makes it worth highlighting and exploring further. The global $(B - I)$ colors of bulge-dominated satellites are, in contrast, largely independent of environment. Likewise, no clear environmental influence is seen for the dispersion around the color profile.

Finally, and not expectedly, at the galaxy mass scales of our study in any environment, bulge-dominated satellites are redder and have shallower color gradients and lower color dispersions relative to disk-dominated satellites.

9.2. Environmental Impact on Disk-dominated Satellites

The colors of *disk-dominated satellites* are more significantly affected by the “local” environment of the host group. At low galaxy stellar masses, $\sim 10^{9.5} M_{\odot}$, the $(B - I)$ colors of disk-dominated satellites are ~ 0.2 mag redder in the centers of galaxy groups ($R < 0.6R_{200}$), relative to similar satellites in the outer regions of the group potentials. This difference is significant at the 95% level as quantified by Kolmogorov–Smirnov test. At the same mass scale disk-dominated galaxies are about 0.1 mag bluer in low-mass groups. No variation with group-centric distance (or any other environment) is seen in the colors of disk-dominated satellites at higher stellar masses.

The median bulge-to-total ratios, integrated above $10^{10} M_{\odot}$ in the disk-dominated satellite samples at $R < 0.6R_{200}$ and $R > 0.6R_{200}$, respectively, are 0.33 and 0.29; the median integrated $(B - I)$ colors of, separately, the disk and bulge components of these two samples, are respectively 1.28 and 1.41 at $R < 0.6R_{200}$ and 1.22 and 1.46 at $R > 0.6R_{200}$. All these values are thus very consistent with each other, within the uncertainties, indicating that the lack of an environmental effect at these high masses is not explained either by bulge-to-total variations or by variations in bulge and/or disk colors between the samples that are being compared. We note, however, that the median bulge half-light radii and disk scale lengths are respectively $1.30^{+0.10}_{-0.06}$ kpc and $2.38^{+0.13}_{-0.08}$ kpc within $0.6R_{200}$, and $1.60^{+0.19}_{-0.10}$ kpc and $3.14^{+0.20}_{-0.13}$ kpc in the outer-group regions, indicating that, in particular, disks of $>10^{10} M_{\odot}$ disk-dominated satellites in the inner cores of groups are $\approx 20\%$ smaller in size, and thus their bulges are more prominent, i.e., less “embedded within the disks,” than is the case at large group-centric distances. This difference is observed at the $>3\sigma$ level; a Kolmogorov–Smirnov test excludes a common parent distribution at the 99% level. The sum of the bulge contribution to the integrated colors may thus dilute the environmental effect with R_{200} on the $(B - I)$ color that is seen at lower masses. We defer a deeper investigation of the colors and sizes of bulge and disk components of ZENS galaxies to a forthcoming publication.

The strongest environmental effect on the disk-dominated satellite population is seen on the color gradients, which are, at fixed galaxy mass $\geq 10^{10} M_{\odot}$, shallower by ≈ -0.15 in high-mass groups and in the dense innermost group regions relative

to less massive groups and to the outer-group regions. Precisely, $\nabla(B - I) \sim -0.25$ in the more massive groups and in the denser group regions, and $\nabla(B - I) \sim -0.4$ in the less massive groups and in the outer regions of groups. Also worth noticing for this population is a hint for a systematic lower color scatter in massive groups relative to lower mass groups (at an integrated statistical significance for $M > 10^{9.5} M_{\odot}$ of 2.5σ); a similar trend, seen at a slightly lower significance in our data, may also be there with group-centric distance, for a lower color scatter in the inner and denser regions of groups relative to the less dense outer-group regions.

In the following we investigate the implications of the strongest environmental effects that we have detected, namely, the color reddening of low-mass disk-dominated satellites inside the cores (relative to the outskirts) of groups, as well as the dependence of their color gradients on both group mass and group-centric distance. In particular, we discuss these environmental effects for the disk-dominated satellite population in the context of stellar population synthesis models, semi-analytic models (SAMs) of galaxy formation, and the “continuity equation” approach of Peng et al. (2010, 2012).

9.3. Interpreting with Stellar Population Models the Environmental Differences in Colors and Color Gradients of Disk-dominated Satellites

Despite the well-known degeneracy of optical colors toward age/metallicity/dust and SFHs, the color difference that we have observed in low-mass disk-dominated satellites as a function of group-centric distance contains information on the origin of such an environmental effect. In particular, while dust¹³ and, to a lesser extent, metallicity, do no doubt play a role, the $(B - I)$ color is quite sensitive to stellar population age variations in spiral galaxies (e.g., MacArthur et al. 2004; Carollo et al. 2007). We thus assumed that the $(B - I)$ colors and color gradients that we have measured are mostly determined by the age of the underlying stellar populations. Despite the substantial uncertainty introduced in the derived age differences by this assumption, the differences provide a useful benchmark to rank stellar population properties, in a relative manner, between and within galaxies. In particular, since we will be comparing galaxy populations of similar Hubble type and stellar mass, the assumption that they have similar dust content and/or SFHs is less uncomfortable than when comparing very different galaxy populations.

In constructing stellar population models for the comparison with the data, we constrained the stellar metallicity using the relation between galaxy stellar mass and stellar metallicity of Gallazzi et al. (2005), which, at the galaxy masses of our ZENS study, gives $Z_{\log M \in [9.5-10]} = 0.004-0.007$, $Z_{\log M \in [10.-10.5]} = 0.01-0.02$, and $Z_{\log M > 10.5} = 0.02-0.03$. To model the observed colors, we used BC03 templates with the above metallicities, a Chabrier (2003) IMF, and the same SFHs as in Table 2; note that the reddest $(B - I)$ colors observed in Figure 17 are obtained only for models with $\tau < 4$ Gyr. We also assessed the impact of different galaxy template models by comparing the BC03-based results with the equivalent estimates based on the 2007 updated version of the original Bruzual & Charlot (2003) libraries (see Bruzual 2007, hereafter CB07).

¹³ We remark that we have not attempted any correction for intrinsic dust absorption within galaxies. In interpreting colors as stellar population (histories) effects, we exclude ZENS galaxies that are mostly affected by internal reddening effects, i.e., galaxies that are strongly star-forming but have red colors (see Section 5.2).

The observed color difference between $\sim 10^{9.5} M_{\odot}$ disk-dominated satellites within and outside $0.6R_{200}$, respectively, is consistent with a median ~ 2 Gyr age difference using either the **CB07** or the **BC03** templates, in the sense of “inner-group” disk-dominated satellites being older than “outer-group” disk-dominated satellites. As a consequence of the inclusion of the thermally pulsating asymptotic giant branch stars, the **CB07** models reach redder colors at shorter times relative to the **BC03** models; thus, the spread around the median value is larger for the former (~ 2 Gyr) than for latter (~ 0.7 Gyr).

An alternative way to interpret the observed color difference between $\sim 10^{9.5} M_{\odot}$ disk-dominated satellites in the inner- and outer-group regions is in terms of a variation of the timescale over which star formation occurs, i.e., in terms of τ variations within the family of exponentially declining SFHs (after fixing the start of star formation activity to the same redshift, z_f , for all galaxies). Using the mass–metallicity relation above, z_f set to 10 Gyr ago, and the **BC03** models, the redder colors of these low-mass disk-dominated satellites in the inner-group regions correspond to ≈ 2 Gyr shorter τ values relative to similar satellites in the outer-group regions (i.e., $\tau_{R>0.6R_{200}} \sim 6$ Gyr versus $\tau_{R<0.6R_{200}} \sim 3\text{--}4$ Gyr). We note that the **CB07** models would give about twice as large τ differences between inner- and outer-group regions.

With a typical galaxy crossing time within a ZENS group $t_{\text{cr}} = R_{200}/v \sim 10^9 \text{ yr } (R_{200}/\text{Mpc}) (\sigma_{\text{los}}/1000 \text{ km s}^{-1})^{-1} \sim 1\text{--}3$ Gyr—where $R_{200} = \sqrt{3}\sigma_{\text{los}}/(10H(z))$, $H(z)$ is the expansion rate of the universe at the median redshift $z = 0.055$ of the ZENS groups, and σ_{los} , i.e., the line-of-sight velocity dispersion of the group, is typically $\sim 200\text{--}400 \text{ km s}^{-1}$ —the estimated τ differences between low-mass disk-dominated satellites in the outer- and inner-group regions are comparable with the timescales of “migration” of these galaxies across their host groups. This interpretation thus supports a picture in which disk-dominated galaxies that plunge into galaxy groups and become satellites within these potentials see their star formation quenched, on timescales $\tau_{\text{quench}} \sim 2$ Gyr, by physical processes that act on the satellites as they migrate toward the cores of the groups. This is in agreement with several other studies (see, e.g., Rasmussen et al. 2012 and references therein).

Following a similar approach, the color gradients of disk-dominated satellites imply differences between the inner and outer galactic regions of (1) $\Delta\tau \sim 1.5$ Gyr and ~ 3 Gyr in the gas-consumption/star formation timescales or (2) $\Delta\text{age} \sim 3$ Gyr and ~ 4 Gyr in the typical age, for galaxies in the cores and outskirts of groups, respectively. In light of their similar nuclear colors (and thus stellar populations), independent of any environment, these comparatively different age variations between inner and outer galactic regions of inner- and outer-group satellites may well indicate quenching of the outer-disk components of satellites in the cores of groups.

Together, the above considerations on the colors and change in strength of the color gradients of disk-dominated satellites lead to a picture where “satellite-quenching” preferentially acts on the outer parts of the disks and occurs on extended timescales of order ~ 2 Gyr as satellites journey toward the centers of their group halos. This is consistent with the picture discussed in Section 8, in which gas is removed from the outer regions of satellite galaxies in groups, causing an enhancement of the central star formation (Koopmann & Kenney 1998; Moss & Whittle 2000).

9.4. Comparisons with a State-of-the-art Semi-analytic Model

SAMs offer an alternative avenue to understand the color difference that we have observed between disk-dominated satellites in the cores and outskirts of groups. Several models have been developed; our scope here is, however, not to perform a complete comparison to identify the model that best fits the data, but, rather, to learn some lessons either from similarities or from differences between observations and a state-of-the-art SAM, which incorporates recipes to ameliorate known deficiencies in previous model generations. We thus focus our data-model comparison entirely on the Guo et al. (2011, hereafter G11) model, which, relative to previous generations of SAMs, substantially improves the description of environmental effects leading to the evolution of satellite galaxies within group halos. In particular, the G11 model implements a relatively less abrupt stripping of gas from satellites and a recipe for disruption of satellites that are stripped of their dark matter halo.

The G11 model was run on the Millennium simulation (Springel et al. 2005), on a box size of 685 Mpc, and has a resolution in galaxy stellar mass of a few $\times 10^9 M_{\odot}$, well suited for a comparison with the ZENS galaxies. G11 used a Chabrier IMF and included a treatment for dust to build the model galaxies. We created 10 random halo samples from all the halos in the G11 volume, matching the mass function of ZENS. From these halo samples we selected satellite galaxies that were classified into two broad morphological types according to a stellar-mass bulge-to-total ratio threshold of $B/T = 0.5$, i.e., $B/T \geq 0.5$ for bulge-dominated galaxies, and $B/T < 0.5$ for disk-dominated galaxies. We note that a similar B/T numerical threshold is used to classify our ZENS sample in similar types, however in I -band light rather than stellar mass; thus, there might be a slight difference in morphological separation when comparing models and ZENS data, which we will keep in mind. Since resolved color gradients are not available for the model, we limit the comparison with the ZENS galaxies to the integrated ($B - I$) colors. Also, the default G11 colors are provided in the SDSS *ugriz* system; hence, a conversion to ($B - I$) was obtained using Table 2 of Blanton & Roweis (2007).

In virtually all semi-analytic computations, galaxies are found to be too red compared to real galaxies, a red-color excess that is interpreted as arising from the combination of a too fast gas consumption through star formation in the early phases of galaxy evolution relative to SFHs of real galaxies, coupled with an excessive stripping of the hot gas when the galaxies are accreted onto a group halo (e.g., Weinmann et al. 2006, 2010; Font et al. 2008; Kimm et al. 2009; Fontanot et al. 2009). As mentioned above, the G11 model includes an improved treatment of stripping of hot gas experienced by galaxies once they become satellites of larger halos. As in other SAMs, the hot-gas stripping in G11 happens after the galaxy enters the virial radius of the group. However, in contrast with earlier generations of models, in which the whole hot gas reservoir is instantaneously removed, in the G11 model only the gas outside a characteristic radius $R_{\text{stripping}}$ within the satellite’s own subhalo is removed (with $R_{\text{stripping}}$ set equal to the smallest between the tidal radius, in the group potential, of the dark matter component of the satellite’s subhalo and the radius at which ram-pressure stripping within the group potential equals the internal galaxy pressure). Satellites can thus retain a reservoir of hot gas in the G11 model, which keeps sustaining star formation activity after they enter the group virial radius. This helps reduce the (progressively larger at progressively lower masses) excess of

red quenched galaxies that is typically observed with respect to the observations in semi-analytic computations.

Galaxies in the **G11** model remain nevertheless too red relative to real galaxies, as shown in the upper panels of Figure 17, where the model colors are shown in comparison with our ZENS data. Specifically, magenta and purple lines are the model median colors for disk-dominated satellites outside and within $0.6R_{200}$, respectively; dashed and solid curves describe models with and without dust reddening. The hatched lines are equivalent to the 1σ dispersion around the median, obtained from the 16th and 84th percentiles.

It is a success of the model and a valuable insight for understanding our results that the **G11** model colors of disk-dominated satellites show similar environmental trends with group mass and group-centric distance as similar ZENS satellites. In the model, at constant galaxy mass, these satellites show colors that are almost independent of group mass; they become, however, substantially redder toward the group centers relative to the groups outskirts. Although not explicitly discussed in **G11**, this is likely due to a feature that seems to be common to several SAMs (including some earlier versions of the **G11** model, on which the latter is based; e.g., De Lucia & Blaizot 2007), as well as to dark-matter-only simulations (Gao et al. 2004): satellites that inhabit the group centers have entered the group virial radius at earlier times t_{infall} relative to satellites that are found in the outskirts of the groups. This “time delay” is typically of order $\Delta t_{\text{infall}} \sim 2\text{--}4$ Gyr (at least in the De Lucia & Blaizot 2007 model, as analyzed by De Lucia et al. 2012); this implies a relatively larger gas consumption and/or loss in the inner-group relative to the outer-group satellites. Similar trends for satellites’ t_{infall} as a function of group-centric distance are also found in hydrodynamical simulations reproducing $z \sim 0$, $\sim 10^{13} M_{\odot}$ galaxy groups within a Λ CDM cosmology (Feldmann et al. 2011).

The **G11** model furthermore also reproduces the fact that the color reddening of disk-dominated satellites in inner- (relative to outer-) group regions is marginally larger at lower (relative to higher) galaxy stellar masses. In the models this can be explained with a Δt_{infall} that decreases with increasing mass (from ~ 4 Gyr at $\sim 10^9 M_{\odot}$ to ~ 2 Gyr at $\sim 10^{11} M_{\odot}$ in the De Lucia et al. 2012 analysis), although a more efficient dynamical friction for high-mass galaxies quickly moves these toward the inner-group regions. In other words, low(er) mass galaxies are subject to the effects of ram-pressure stripping for a factor >2 longer time periods than the more massive satellites.

There are, however, also important discrepancies between the **G11** model and the ZENS data that are as illuminating as the successes highlighted above.

1. First, as already stressed above, the **G11** model predicts colors that are still significantly redder than real satellite galaxies at any galaxy mass of our study. In the models with no dust reddening and at $M < 10^{10} M_{\odot}$, the discrepancy is of $\approx 0.4\text{--}0.5$ mag and grows to ≈ 0.7 mag for the models with dust. A strictly quantitative comparison between data and models is difficult due to the slightly different morphological selection criteria and the intervening conversion fractions for the colors discussed above. The size of the discrepancy is, however, substantial. Furthermore, a similar discrepancy between model and SDSS data is already highlighted for the $u - i$ color in Figure 12 of **G11**, especially at stellar masses $\sim 10^{9.5} M_{\odot}$. We are thus confident of a genuine shift in color between the model and the data in the direction of the model satellites being indeed redder than the ZENS satellites. This residual reddening

of the **G11** model relative to the ZENS data indicates that further revision of the model is required, most likely in the past SFHs of present-day galaxies, so as to avoid gas over-consumption at early times while at the same time preventing excessive residual gas in galaxies at these mass scales at redshift $z = 0$.

We note that De Lucia et al. (2012) have recently stressed the importance of properly relating galaxies’ properties to their past environmental history, i.e., to the evolution of the host halo environment of galaxies with different masses and redshifts of infall into the final halos. These authors infer the timescales for environmental quenching of satellite galaxies using merger trees to link the observed passive fraction with the fraction of galaxies of a given mass that spend a given amount of time in the group/cluster environment. Predictions for colors of galaxies in this model are not available. The employed merger trees are, however, similar to those adopted in the **G11** model; thus, we suspect that despite this model offering alternative ways to measure the timescale of environmental quenching and to interpret observed trends with environment, it will likely show a similar color discrepancy relative to our data.

2. Furthermore, the model shows a stronger flattening of the color versus galaxy mass relation than the real data: model colors remain essentially constant over the whole mass range of our analysis, with at most a $\lesssim 0.1$ mag reddening toward higher masses, while ZENS satellites show a reddening of ~ 0.3 mag over the same mass range. This indicates that the modification to the SFHs in model galaxies needs to be a function of galaxy stellar mass.
3. Finally, on quantitative ground, while the amount by which inner-group satellites are redder than outer-group satellites for low-mass $\sim 10^{9.5} M_{\odot}$ satellites is similar (~ 0.2 mag) between the observations and the model, at higher galaxy masses the latter shows a larger color difference between these two populations than the ZENS data. Possible interpretations of this discrepancy may be that, in the model, ram-pressure effects on massive galaxies, and/or their dynamical friction timescales, are overestimated compared with ram pressure and timescales in the universe. Alternatively, massive disk-dominated satellites in the real universe may continue accreting gas also when close to the group centers, in contrast with the model assumption that no gas accretion on satellites takes place after they enter the virtualized group regions.

9.5. Interpreting Environmental Trends in Colors and Color Gradients of Disk-dominated Satellites within a Continuity-equation Approach

The Peng et al. (2010) continuity approach to analyzing galaxy evolution has produced an impressively self-consistent picture of the overall evolution of the active and quenched galaxy populations since $z \sim 2$. Within the framework of this approach, Peng et al. (2010) studied a large sample of groups in the SDSS. Although this methodology has been hitherto applied primarily to the integrated quantities of mass and SFR, rather than morphology, it is nevertheless worth comparing the results of this section, and especially those concerning the overall $(B - I)$ colors of the galaxies (the upper panels in Figure 17), with those in Peng et al. (2010).

The independence of overall $(B - I)$ color for disk galaxies on group halo mass and the dependence, especially at low masses, on group-centric distance are consistent with the finding

by Peng et al. (2010) that the red fraction of satellites depends on local density within a group, but not on halo mass (at fixed density). The increasing impact of the group-centric radius environment with decreasing stellar mass of the galaxies is also consistent with the different characteristics of Peng et al.’s “mass-quenching” and “environment-quenching” processes. The rate of the former depends on the SFR, which is broadly proportional to the mass of star-forming galaxies, whereas the latter is, from the separability of the red fractions, independent of the stellar mass. Environment quenching thus dominates over mass quenching at lower stellar masses, and especially so below $10^{10} M_{\odot}$.

The precise morphological mix in the quenched fractions of satellites in different environments will be further discussed in Paper IV (C. M. Carollo et al., in preparation).

10. SUMMARY AND CONCLUDING REMARKS

We have presented photometric measurements for the 1484 galaxies in the sample of 141 ZENS groups. All measurements presented in this paper are included in the ZENS catalog published in Paper I. Photometric galaxy parameters include total ($B - I$) colors, color gradients, color dispersions, and galaxy stellar masses and SFRs, as well as bulge and disk ($B - I$) colors and stellar masses, the latter based on the parametric bulge+disk decompositions in B and I presented in Paper II. Voronoi-tesselated two-dimensional ($B - I$) color maps extending out to \sim two galaxy half-light radii were also obtained. ZENS galaxies were classified in the three spectral types of quenched, moderately star-forming, and strongly star-forming systems, based on a spectral classification scheme using the combination of spectral absorption/emission features, broadband (FUV) NUV–optical colors, and SED fits to the available photometric data. The combination of multiple probes of star formation enables an efficient separation of red, quenched systems from dust-reddened star-forming galaxies; at $\sim 10^{10} M_{\odot}$, the latter are found to contribute up to 50% to the ($B - I$) red sequence.

In the ZENS sample as in others (see, e.g., Peletier et al. 1990; de Jong 1996; Jansen et al. 2000; Taylor et al. 2005; Gonzalez-Perez et al. 2011; Tortora et al. 2010):

1. the average ($B - I$) colors at the half-light radius steadily increase with galaxy stellar mass and toward earlier types;
2. the intensity of ($B - I$) color gradients correlates with morphological type, as defined using the structural parameters and morphological classification of Paper II: E/S0 galaxies have [$\nabla(B - I) \sim -0.1$]; and bulge-dominated spiral galaxies instead have [$\nabla(B - I) \sim -0.2$]; and
3. most galaxies have negative color gradients (centers redder than outskirts); a non-negligible fraction of galaxies shows, however, flat or positive color gradients. At $M \sim 10^{10} M_{\odot}$, about 20% of galaxies of all morphological types have cores that are bluer than the outer galactic regions; the fraction of galaxies with inverted color gradients increases with decreasing galaxy stellar mass. Interestingly, in bulge-dominated galaxies, the inversion of the color profiles is also accompanied by an enhancement of the median sSFR with respect to galaxies with the same morphology but normal (non-inverted) profiles; in contrast, positive and negative color gradients in disk-dominated galaxies have comparable sSFRs. Evidence for centrally concentrated star formation in groups and clusters, especially relative to the field population, has been suggested to be the outcome of

tidal perturbations or ram-pressure removal of the outer gas reservoir, leading to an enhancement of the star formation in the galaxy cores (e.g., Koopmann & Kenney 1998; Moss & Whittle 2000; Bartholomew et al. 2001; Rose et al. 2001). Bahé et al. (2013) have recently suggested that ram-pressure stripping may be already at work even outside of the group’s virial radius.

We find that, above the level of stellar mass completeness of our sample, the median mass of galaxies of a given morphological type, and especially of disk-dominated satellite galaxies, does not depend substantially on any environment, including the halo mass. This is in agreement with the constancy of the characteristic M^* in the Schechter (Schechter 1976) mass function of satellite galaxies over a wide range of halo masses, which indicates that mass quenching of satellites is independent of halo mass.

Focusing on *disk satellites* only, we have investigated, at fixed stellar mass and Hubble type, the dependence on group mass, distance from the group center, and LSS overdensity of ($B - I$) colors, color gradients, and color dispersions around the mean gradients. Our findings are summarized as follows.

1. Bulge-dominated satellites have redder colors, shallower color gradients, and smaller color scatter than disk-dominated satellites of similar masses in similar environments. Our data suggest that color gradients of bulge-dominated satellites may be shallower in regions of low environmental density—i.e., outer-group regions and low LSS overdensities—compared to the same Hubble type satellites in the corresponding denser environments.
2. The group environment has a noticeable effect on both colors and color gradients of disk-dominated satellites. These satellites have shallower ($B - I$) color gradients, by about -0.2 dex, in the inner-group regions relative to regions at larger group-centric distances, and at high group masses relative to lower group masses. Furthermore, at galaxy masses $< 10^{10} M_{\odot}$, disk-dominated satellites in our sample have ~ 0.2 mag redder ($B - I$) colors in the inner-group regions relative to similar satellites in the outer-group regions.

A stellar population analysis applied to the environmental differences in ($B - I$) colors and color gradients detected for disk-dominated ZENS satellites indicates star formation timescales $\tau \sim 2$ Gyr shorter, or ~ 2 Gyr older stellar populations, for low-mass disk-dominated satellites in the cores of groups relative to the group outskirts. These timescales are comparable with the timescales of satellite infall within the inner-group regions.

Similar long τ_{quench} to those inferred above are found by other independent studies, which also estimate of order a couple billion years for physical processes within the groups to act (e.g., Balogh et al. 2000; Wang et al. 2007; Weinmann et al. 2009; von der Linden et al. 2010; McGee et al. 2011; Kovač et al. 2010; Feldmann et al. 2010, 2011; Rasmussen et al. 2012). In the semi-analytic study of De Lucia et al. (2012), the observations can be reproduced if the passivization occurs on even longer timescales of $\sim 5-7$ Gyr. Also numerical simulations of gas stripping in groups and clusters support a scenario in which galaxies are depleted of their hot gas in a gradual manner while they orbit in the group potential. As shown by McCarthy et al. (2008), satellites can retain a substantial fraction of the hot halo and thus sustain some level of star formation up to 10 Gyr after the infall in the group.

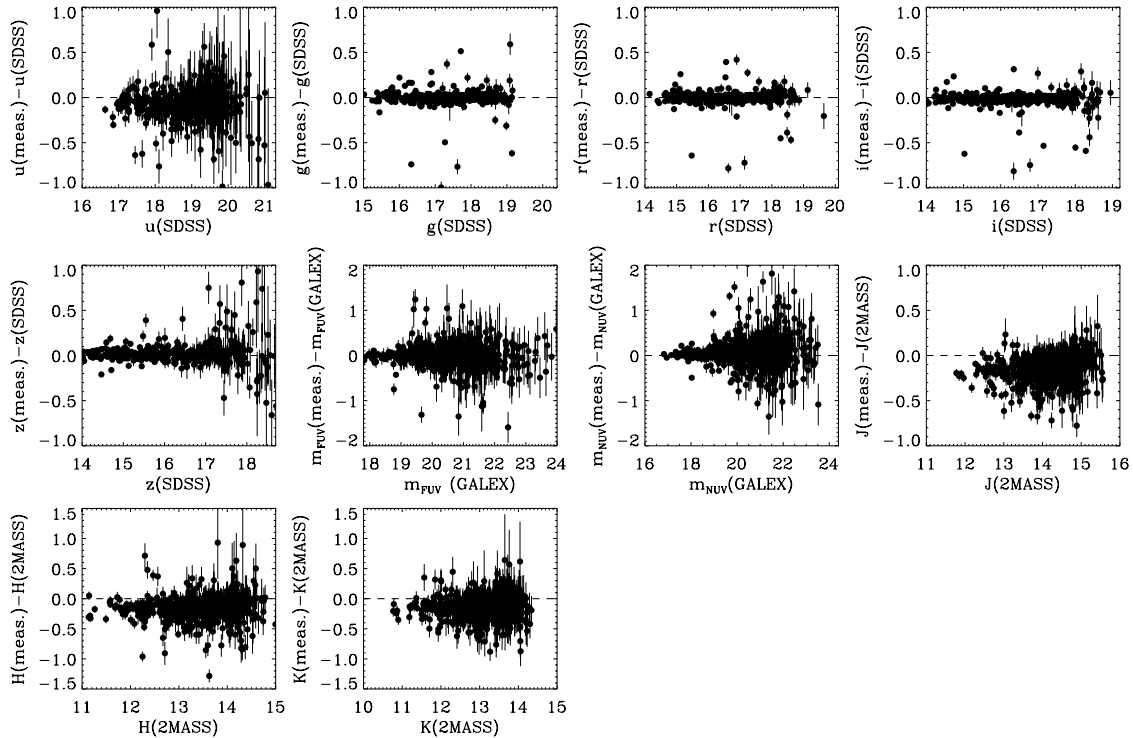


Figure 18. Comparison between the magnitudes that we measured on the public *GALEX*, *SDSS*, and *2MASS* images (indicated with “meas.”) and the magnitudes published by the survey teams (indicated with the names of the various surveys) for the ZENS galaxies for which such data are available. The *mag(GALEX)* and *mag(2MASS)* data points refer to Kron (Kron 1980) magnitudes, and the *mag(SDSS)* data points to Petrosian fluxes; the latter are based on circular apertures. Our own measurements are performed on elliptical apertures with a semi-major axis equal to twice the largest between the WFI *B*- and *I*-band Petrosian radii.

We note that Wetzel et al. (2012a, 2012b) report shorter timescales for suppression of star formation relative to this previous work and our own estimate. In particular, Wetzel et al. (2012b) suggest a two-phase satellite-quenching process, characterized by a $\sim 2\text{--}4$ Gyr period after a galaxy enters the virialized group potential, in which its star formation is unaffected by the group environment, followed by a rapid truncation of star formation in a short < 0.8 Gyr event. These authors use an *indirectly* derived strong redshift evolution of the fraction of quenched satellite galaxies, grounded on the combination of heterogeneous data sets at low and high redshifts. This strong evolution is, however, at odds with several other studies that self-consistently sample this evolution within large, homogenous datasets (e.g., Knobel et al. 2012; Ilbert et al. 2013). We suspect that inputting in the Wetzel et al. analysis a milder evolution of the fraction of quenched satellites at fixed stellar mass, as directly indicated by the data, could reconcile their estimates for the quenching timescales with those inferred from the present analysis and the several other quoted works.

Semi-analytical model predictions also point indeed at inner-group satellites to have an ~ 2 Gyr earlier infall time—and consequently an earlier star formation quenching through loss of the hot gas reservoir, and gas consumption in star formation—than outer-group satellites. A quantitative comparison shows, however, that even the Guo et al. (2011) model, which incorporates a progressive effect of ram pressure, still produces too red colors of satellite galaxies at the explored mass scales and Hubble types relative to the observations. A modification of the model is required so as to avoid excessive gas over-consumption at early times and, simultaneously, excessive residual gas in galaxies at redshift $z = 0$; most likely, both the SFHs of galaxies and the feedback recipe need modifications. Such modifications need to

be a function of galaxy stellar mass in order to reproduce the trends observed in the ZENS data.

The mass scales $\lesssim 10^{10} M_{\odot}$ at which disk-dominated satellites most evidently show a reddening of their $(B - I)$ colors with decreasing distance from the group center are those shown by Peng et al. (2010) to be, at $z = 0$, mostly affected by environment quenching. This quenching process has been further shown by Peng et al. (2012) to be practically entirely due to environmental effects on galaxies as they become satellites of virialized groups. Redder colors in high-density environments are explained through quenching of star formation in the satellite galaxy population, not in central galaxies (i.e., by “satellite quenching”). The ZENS satellites’ analysis that we have presented adds further evidence to this scenario. In particular, our analysis supports that the environment affects galaxy evolution below a galaxy mass scale of $\approx 10^{10.5} M_{\odot}$ through physics that occurs within the group halos (van den Bosch et al. 2008; Weinmann et al. 2009; Guo et al. 2009; Peng et al. 2010). The fact that the strongest variation in the colors of low-mass disk-dominated satellites is observed as a function of the location within groups points to a physical mechanism for the “satellite quenching” that either depends on the local density rather than the global halo potential or affects the gas inflow, outflow, and/or content of galaxies as they sink as satellites in the potentials of their host groups.

A.C., E.C., and C.R. acknowledge support from the Swiss National Science Foundation. This publication makes use of data from ESO Large Program 177.A-0680. This publication makes use of data products from the Two Micron All Sky Survey, which is a joint project of the University of Massachusetts and the Infrared Processing and Analysis Center/California

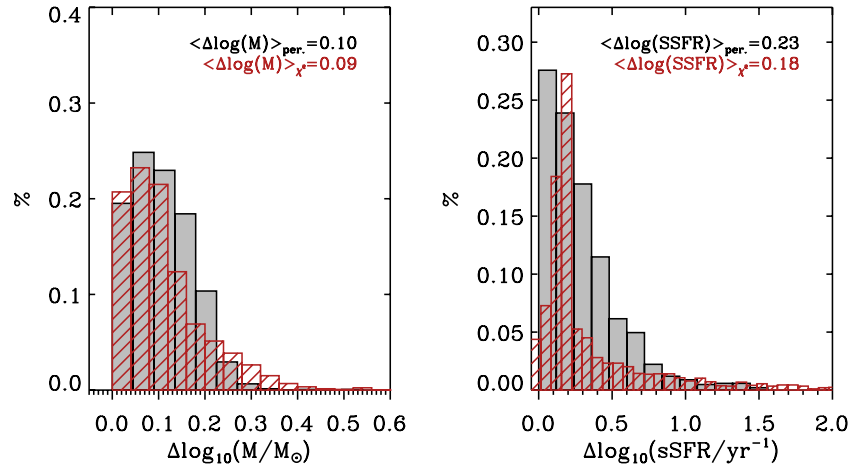


Figure 19. Distributions of the errors for the stellar masses and sSFRs obtained from the ZEBRA+ SED fits. The gray histograms are for errors on the parameters calculated from the 16th and 84th percentiles of the likelihood distributions of the complete set of templates used in the fit. The black hatched histograms (red in the online version) show the typical uncertainties that are obtained by determining the values of the considered parameters that correspond to an increase of 50% in the value of χ^2 with respect to the minimum χ^2 of the best-fit templates. The corresponding median errors are indicated at the top of each panel.

(A color version of this figure is available in the online journal.)

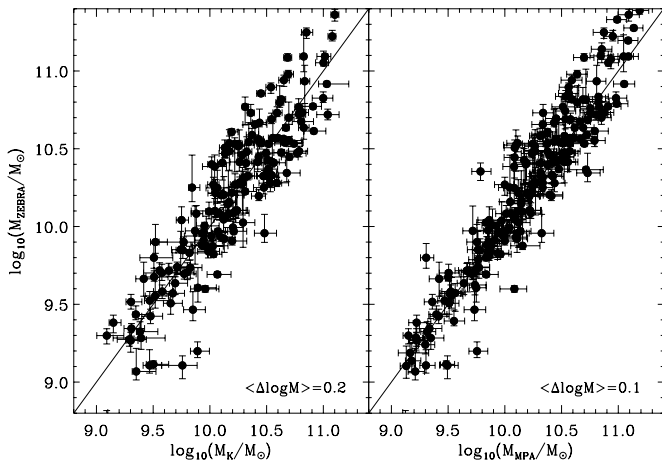


Figure 20. Comparison between stellar masses available in the literature and best-fit masses measured by us with ZEBRA+ for a subsample of ZENS galaxies. The left panel shows the comparison with the SDSS DR4 (Kauffmann et al. 2003b) mass estimates based on the analysis of spectra absorption lines. The right panel shows the comparison with the DR7 masses based on photometric fits (see Salim et al. 2007). The median mass difference between our ZEBRA+ masses and the published ones is in both cases reported at the bottom right corner of the panel.

Institute of Technology, funded by the National Aeronautics and Space Administration and the National Science Foundation. *GALEX* (*Galaxy Evolution Explorer*) is a NASA Small Explorer, launched in 2003 April. We gratefully acknowledge NASA’s support for construction, operation, and science analysis for the *GALEX* mission.

APPENDIX

RELIABILITY OF THE SED FITS

In this [Appendix](#) we present the tests that we performed to assess the reliability of the photometric data sets, which is used as input for the SED fits, and the robustness of the resulting mass estimates provided by ZEBRA+.

A.1. Impact of Photometric Errors on Derived Quantities

In [Figure 18](#) we compare the magnitudes that we obtained by applying the aperture photometry described in [Section 3.1](#) with the public measurements from the various surveys databases.

The agreement is generally good, and deviations are in all cases smaller than 0.1 mag. There are, however, some systematic effects: our SDSS and 2MASS magnitudes are slightly brighter than the published values. We have tested that this is partly due to our use of a larger aperture, indicating some flux losses in the published measurements. We also note that SDSS magnitudes are calculated using a circular aperture and hence part of the observed scatter stems from different aperture geometry. In fact, some of the most highly deviant points occur for highly inclined galaxies, for which the SDSS circular aperture was observed to miss a large fraction of the flux. Note also that a larger scatter in the magnitudes is observed for the *GALEX*-UV and SDSS *u/z* filters, which are noise dominated.

Given the heterogeneous nature and origin of our photometry, the size of the PSF FWHM varies rather strongly across the probed wavelength range: from $\sim 5''$ for the *GALEX* UV data to sub-arcsecond resolution under the best observing condition for our own *I*-band imaging. In principle, a matching of the images from the different surveys to a common PSF scale would be required to derive consistent color measurements. The use of a relatively large aperture ($2 \times R_p$) in the calculation of the magnitudes, however, effectively reduces PSF-related biases. Indeed, we tested on simulated data that degrading the quality of the images with the best PSF to the worst PSF increased rather than decreased the size of the errors on the derived quantities. Furthermore, we also checked on simulated images that using variable apertures in the different passbands does not improve the determination of stellar masses and other derived quantities due to two effects, namely, the increased noise in the degraded images and a residual contamination from nearby companions. As a final test for the reliability of our derived magnitudes, we smoothed the WFI *I*-band images—which have, on average, the best resolution—with a Gaussian kernel to reach a homogeneous 5 arcsec PSF. We then re-measured on these smoothed images the flux inside the same Petrosian aperture used to derive the stellar masses in [Section 3.1](#) and compared the resulting luminosities with the ones obtained from the unconvolved images. For about three-quarters of the sample, the effect of PSF blurring causes flux variations that are within the average photometric error in the *I* filter; furthermore, the difference remains within 0.1 mag for about 90% of the sample. In the remaining few cases, differences of up to about 0.3 mag

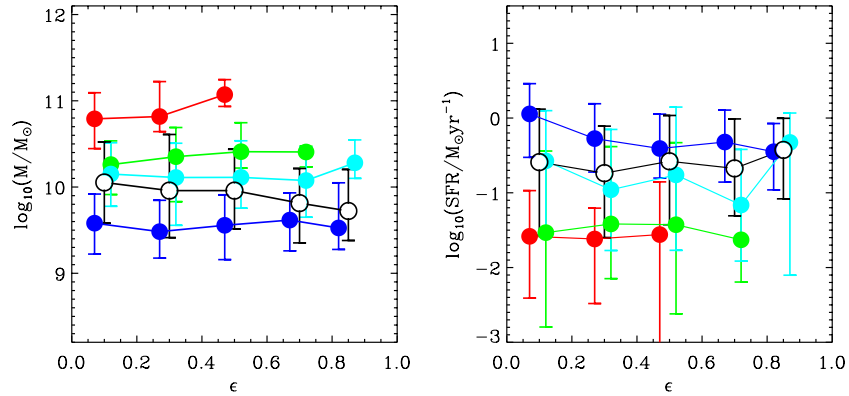


Figure 21. Median galaxy stellar mass and SFR as a function of ellipticity. Symbols with error bars are the median, in five ellipticity bins, for the global galaxy sample (stars, black in the online version), and for morphologically split samples of E/S0 galaxies (black, red in the online version), bulge-dominated spirals (dark gray, green in the online version), intermediate-type disks (gray, cyan in the online version), and late-type disks (empty circles, blue in the online version). Error bars show the 25th and 75th percentiles of the distributions. Ellipticities and morphological classes are taken from Paper II.

(A color version of this figure is available in the online journal.)

were observed both in the positive and in the negative direction, indicating that both flux losses and increased noise have an impact in this measurement. In these cases, the approach of deriving the galaxy fluxes on the original images guarantees higher quality measurements. We are therefore confident that the adopted scheme for measuring galaxy fluxes delivers stellar masses and related quantities that are robust to PSF variations across the spectral region of the used imaging data set.

A.2. Errors on the ZEBRA+ Stellar Masses and (s)SFRs, and Comparisons with the Literature

To derive an uncertainty on the parameters obtained from the ZEBRA+ fits, we utilized the likelihood and χ^2 distributions of the relevant quantities (masses, SFRs, sSFRs, etc.) from the full set of the employed templates. Specifically, we derived the errors in two different ways, i.e., (1) using the 16th and 84th percentiles of the global likelihood distributions as our uncertainty measure and (2) deriving the values of the considered parameters that bracket an increase of 50% in χ^2 with respect to the χ^2 of the best-fit template. We show the calculated errors in Figure 19 for galaxy masses and SFRs. The median error on the galaxy mass is ~ 0.1 dex and ~ 0.2 dex for the sSFRs. As expected, (specific) SFRs are subject to larger uncertainties than the masses; hence, our careful inspection of the spectral lines and color-color diagrams outlined in Section 5 to define the quenched and star-forming populations substantially improves the purity of these samples relative to a simple cut in (SED-fit-based) sSFR.

As a further indication of the robustness of our stellar masses, we can use published measurements for a direct comparison. For about 200 galaxies in our sample, stellar masses are available from SDSS DR4 (Kauffmann et al. 2003b; derived from stellar absorption lines) and DR7 (Salim et al. 2007; calculated from fits to the photometry) analyses. In Figure 20 we show the comparison between these published masses and ours, estimated with ZEBRA+ SED fits. Figure 20 shows a good agreement between our masses and the values in the literature, with typical scatter of about 0.1–0.2 dex, consistent with the estimate calculated from the ZEBRA likelihoods. At a conservative 3σ level, the scatter in the stellar mass estimates is ~ 0.6 , i.e., remains within a factor of four in the worst cases.

A.3. Inclination Effects

The derived photometric quantities need to be checked for a possible dependence on inclination (i.e., ellipticity). The light

absorption by the interstellar dust is more severe at shorter wavelengths than in the red part of the spectrum, and hence a poor treatment of the internal dust extinction could lead to fitting highly inclined galaxies with preferentially older, less active—hence redder—templates than those used for face-on galaxies. Maller et al. (2009), for example, show a systematic offset in the estimates of stellar masses for edge-on and face-on galaxies in the SDSS analysis of Kauffmann et al. (2003b; we do not detect this effect in our comparison above due to the rather limited number of galaxies in the comparison).

Using the structural parameters and morphological classifications presented in Paper II, in Figure 21 we show the ZEBRA+ galaxy masses and SFRs as a function of the measured galaxy ellipticity, both for the full sample of galaxies and also splitting the sample by morphological type. Considering the global sample, we find a slight decrease of stellar masses with ellipticity: looking at the morphological type separately, however, we see that the median mass is remarkably flat with increasing galaxy elongation, and the aforementioned trend is simply a consequence of a changing morphological mix at a given axis ratio plus a different mass function of galaxy types. Regarding the SFR, there is a very modest decrease of the median SFR with ellipticity for late disk galaxies only, although the distributions for face-on and edge-on galaxies are statistically consistent. The other morphological types do not show any trends of masses and SFRs with ellipticity. We conclude that our estimates of (s)SFRs and stellar masses are not significantly biased with ellipticity.

REFERENCES

- Abazajian, K. N., Adelman-McCarthy, J. K., Agüeros, M. A., et al. 2009, *ApJS*, 182, 543
- Annibali, F., Bressan, A., Rampazzo, R., et al. 2010, *A&A*, 519, A40
- Bahé, Y. M., McCarthy, I. G., Balogh, M. L., & Font, A. S. 2013, *MNRAS*, 430, 3017
- Baldry, I. K., Balogh, M. L., Bower, R. G., et al. 2006, *MNRAS*, 373, 469
- Baldwin, J. A., Phillips, M. M., & Terlevich, R. 1981, *PASP*, 93, 5
- Balogh, M. L., Baldry, I. K., Nichol, R., et al. 2004, *ApJL*, 615, L101
- Balogh, M. L., Navarro, J. F., & Morris, S. L. 2000, *ApJ*, 540, 113
- Bamford, S. P., Nichol, R. C., Baldry, I. K., et al. 2009, *MNRAS*, 393, 1324
- Bartholomew, L. J., Rose, J. A., Gaba, A. E., & Caldwell, N. 2001, *AJ*, 122, 2913
- Bell, E. F., McIntosh, D. H., Barden, M., et al. 2004, *ApJL*, 600, L11
- Bertin, E., & Arnouts, S. 1996, *A&AS*, 117, 393
- Biviano, A., Katgert, P., Thomas, T., & Adami, C. 2002, *A&A*, 387, 8
- Blanton, M. R., & Roweis, S. 2007, *AJ*, 133, 734
- Bolzonella, M., Kovač, K., Pozzetti, L., et al. 2010, *A&A*, 524, A76
- Brinchmann, J., Charlot, S., White, S. D. M., et al. 2004, *MNRAS*, 351, 1151

- Bruzual, A. G. 2007, *IAU Symposium*, 241, 125
- Bruzual, G., & Charlot, S. 2003, *MNRAS*, 344, 1000
- Bundy, K., Ellis, R. S., Conselice, C. J., et al. 2006, *ApJ*, 651, 120
- Bundy, K., Scarlata, C., Carollo, C. M., et al. 2010, *ApJ*, 719, 1969
- Caldwell, N. 1984, *PASP*, 96, 287
- Calvi, R., Poggianti, B. M., Fasano, G., & Vulcani, B. 2012, *MNRAS*, 419, L14
- Calzetti, D., Armus, L., Bohlin, R. C., et al. 2000, *ApJ*, 533, 682
- Cameron, E. 2011, *PASA*, 28, 128
- Cappellari, M., & Copin, Y. 2003, *MNRAS*, 342, 345
- Cardelli, J. A., Clayton, G. C., & Mathis, J. S. 1989, *ApJ*, 345, 245
- Carollo, C. M., Cibinel, A., Lilly, S. J., et al. 2013, *ApJ*, 776, 71 (Paper I)
- Carollo, C. M., Scarlata, C., Stiavelli, M., Wyse, R. F. G., & Mayer, L. 2007, *ApJ*, 658, 960
- Cattaneo, A., Dekel, A., Devriendt, J., Guiderdoni, B., & Blaizot, J. 2006, *MNRAS*, 370, 1651
- Cen, R. 2011, *ApJ*, 741, 99
- Chabrier, G. 2003, *PASP*, 115, 763
- Cibinel, A., Carollo, C. M., Lilly, S. J., et al. 2013, *ApJ*, 776, 72 (Paper II)
- Colless, M., Dalton, G., Maddox, S., et al. 2001, *MNRAS*, 328, 1039
- Couch, W. J., & Sharples, R. M. 1987, *MNRAS*, 229, 423
- Crain, R. A., Theuns, T., Dalla Vecchia, C., et al. 2009, *MNRAS*, 399, 1773
- Croton, D. J., Farrar, G. R., Norberg, P., et al. 2005, *MNRAS*, 356, 1155
- Daigle, O., Carignan, C., Amram, P., et al. 2006, *MNRAS*, 367, 469
- Davis, M., Gerke, B. F., Newman, J. A., & Deep2 Team, 2005, in ASP Conf. Ser. 339, *Observing Dark Energy*, ed. S. C. Wolff & T. R. Lauer (San Francisco, CA: ASP), 128
- Davoodi, P., Pozzi, F., Oliver, S., et al. 2006, *MNRAS*, 371, 1113
- de Jong, R. S. 1996, *A&A*, 313, 377
- Dekel, A., & Birnboim, Y. 2006, *MNRAS*, 368, 2
- De Lucia, G., & Blaizot, J. 2007, *MNRAS*, 375, 2
- De Lucia, G., Weinmann, S., Poggianti, B. M., Aragón-Salamanca, A., & Zaritsky, D. 2012, *MNRAS*, 423, 1277
- Diehl, S., & Statler, T. S. 2006, *MNRAS*, 368, 497
- Dressler, A. 1980, *ApJ*, 236, 351
- Dressler, A., & Gunn, J. E. 1983, *ApJ*, 270, 7
- Ebeling, H., White, D. A., & Rangarajan, F. V. N. 2006, *MNRAS*, 368, 65
- Eke, V. R., Baugh, C. M., Cole, S., et al. 2004, *MNRAS*, 348, 866
- Feldmann, R., Carollo, C. M., & Mayer, L. 2011, *ApJ*, 736, 88
- Feldmann, R., Carollo, C. M., Mayer, L., et al. 2010, *ApJ*, 709, 218
- Feldmann, R., Carollo, C. M., Porciani, C., et al. 2006, *MNRAS*, 372, 565
- Ferreira, I., Lisker, T., Carollo, C. M., Lilly, S. J., & Mobasher, B. 2005, *ApJ*, 635, 243
- Font, A. S., Bower, R. G., McCarthy, I. G., et al. 2008, *MNRAS*, 389, 1619
- Fontanot, F., De Lucia, G., Monaco, P., Somerville, R. S., & Santini, P. 2009, *MNRAS*, 397, 1776
- Gallazzi, A., Charlot, S., Brinchmann, J., White, S. D. M., & Tremonti, C. A. 2005, *MNRAS*, 362, 41
- Gao, L., Springel, V., & White, S. D. M. 2005, *MNRAS*, 363, L66
- Gao, L., White, S. D. M., Jenkins, A., Stoehr, F., & Springel, V. 2004, *MNRAS*, 355, 819
- Gil de Paz, A., Boissier, S., Madore, B. F., et al. 2007, *ApJS*, 173, 185
- Giodini, S., Finoguenov, A., Pierini, D., et al. 2012, *A&A*, 538, A104
- Gonzalez-Perez, V., Castander, F. J., & Kauffmann, G. 2011, *MNRAS*, 411, 1151
- Gunn, J. E., & Gott, J. R., III. 1972, *ApJ*, 176, 1
- Guo, Q., White, S., Boylan-Kolchin, M., et al. 2011, *MNRAS*, 413, 101
- Guo, Y., McIntosh, D. H., Mo, H. J., et al. 2009, *MNRAS*, 398, 1129
- Hahn, O., Porciani, C., Carollo, C. M., & Dekel, A. 2007, *MNRAS*, 375, 489
- Hahn, O., Porciani, C., Dekel, A., & Carollo, C. M. 2009, *MNRAS*, 398, 1742
- Haines, C. P., Gargiulo, A., & Merluzzi, P. 2008, *MNRAS*, 385, 1201
- Heckman, T. M. 1980, *A&A*, 87, 152
- Ilbert, O., McCracken, H. J., Le Fevre, O., et al. 2013, *A&A*, 556, A55
- Ilbert, O., Salvato, M., Le Floch, E., et al. 2010, *ApJ*, 709, 644
- Jansen, R. A., Franx, M., Fabricant, D., & Caldwell, N. 2000, *ApJS*, 126, 271
- Kauffmann, G., Heckman, T. M., Tremonti, C., et al. 2003a, *MNRAS*, 346, 1055
- Kauffmann, G., Heckman, T. M., White, S. D. M., et al. 2003b, *MNRAS*, 341, 33
- Kawata, D., & Mulchaey, J. S. 2008, *ApJL*, 672, L103
- Khochfar, S., & Ostriker, J. P. 2008, *ApJ*, 680, 54
- Kimm, T., Somerville, R. S., Yi, S. K., et al. 2009, *MNRAS*, 394, 1131
- Knobel, C., Lilly, S. J., Kovac, K., et al. 2012, *ApJ*, 769, 24
- Koopmann, R. A., & Kenney, J. D. P. 1998, *ApJL*, 497, L75
- Kovač, K., Lilly, S. J., Knobel, C., et al. 2010, *ApJ*, 718, 86
- Kron, R. G. 1980, *ApJS*, 43, 305
- Larson, R. B., Tinsley, B. M., & Caldwell, C. N. 1980, *ApJ*, 237, 692
- Lemaux, B. C., Lubin, L. M., Shapley, A., et al. 2010, *ApJ*, 716, 970
- Lilly, S. J., Le Brun, V., Maier, C., et al. 2009, *ApJS*, 184, 218
- Lilly, S. J., Le Fèvre, O., Renzini, A., et al. 2007, *ApJS*, 172, 70
- MacArthur, L. A., Courteau, S., Bell, E., & Holtzman, J. A. 2004, *ApJS*, 152, 175
- Macchetto, F., Pastoriza, M., Caon, N., et al. 1996, *A&AS*, 120, 463
- Madgwick, D. S., Lahav, O., Baldry, I. K., et al. 2002, *MNRAS*, 333, 133
- Maller, A. H., Berlind, A. A., Blanton, M. R., & Hogg, D. W. 2009, *ApJ*, 691, 394
- Martin, D. C., Fanson, J., Schiminovich, D., et al. 2005, *ApJL*, 619, L1
- Maulbetsch, C., Avila-Reese, V., Colín, P., et al. 2007, *ApJ*, 654, 53
- McCarthy, I. G., Frenk, C. S., Font, A. S., et al. 2008, *MNRAS*, 383, 593
- McGee, S. L., Balogh, M. L., Wilman, D. J., et al. 2011, *MNRAS*, 413, 996
- Moss, C., & Whittle, M. 2000, *MNRAS*, 317, 667
- Newman, J. A., Cooper, M. C., Davis, M., et al. 2013, *ApJS*, 208, 5
- Oemler, A., Jr. 1974, *ApJ*, 194, 1
- Oesch, P. A., Carollo, C. M., Feldmann, R., et al. 2010, *ApJL*, 714, L47
- Oke, J. B. 1974, *ApJS*, 27, 21
- Pannella, M., Gabasch, A., Goranova, Y., et al. 2009, *ApJ*, 701, 787
- Peletier, R. F., Davies, R. L., Illingworth, G. D., Davis, L. E., & Cawson, M. 1990, *AJ*, 100, 1091
- Peng, Y.-j., Lilly, S. J., Kovač, K., et al. 2010, *ApJ*, 721, 193
- Peng, Y.-j., Lilly, S. J., Renzini, A., & Carollo, M. 2012, *ApJ*, 757, 4
- Phillips, M. M., Jenkins, C. R., Dopita, M. A., Sadler, E. M., & Binette, L. 1986, *AJ*, 91, 1062
- Poggianti, B. M., Aragón-Salamanca, A., Zaritsky, D., et al. 2009, *ApJ*, 693, 112
- Poggianti, B. M., Smail, I., Dressler, A., et al. 1999, *ApJ*, 518, 576
- Pozzetti, L., Bolzonella, M., Lamareille, F., et al. 2007, *A&A*, 474, 443
- Pozzetti, L., Bolzonella, M., Zucca, E., et al. 2010, *A&A*, 523, A13
- Pracy, M. B., Driver, S. P., De Propris, R., Couch, W. J., & Nulsen, P. E. J. 2005, *MNRAS*, 364, 1147
- Rasmussen, J., Mulchaey, J. S., Bai, L., et al. 2012, *ApJ*, 757, 122
- Rose, J. A., Gaba, A. E., Caldwell, N., & Chaboyer, B. 2001, *AJ*, 121, 793
- Salim, S., Rich, R. M., Charlot, S., et al. 2007, *ApJS*, 173, 267
- Sanders, J. S., & Fabian, A. C. 2001, *MNRAS*, 325, 178
- Schechter, P. 1976, *ApJ*, 203, 297
- Schlegel, D. J., Finkbeiner, D. P., & Davis, M. 1998, *ApJ*, 500, 525
- Sersic, J. L. 1968, *Atlas de galaxias australes (Cordoba, Argentina: Observatorio Astronomico)*
- Sheth, R. K., & Tormen, G. 2004, *MNRAS*, 350, 1385
- Simard, L., Willmer, C. N. A., Vogt, N. P., et al. 2002, *ApJS*, 142, 1
- Skibba, R. A. 2009, *MNRAS*, 392, 1467
- Skrutskie, M. F., Cutri, R. M., Stiening, R., et al. 2006, *AJ*, 131, 1163
- Springel, V., White, S. D. M., Jenkins, A., et al. 2005, *Natur*, 435, 629
- Taylor, V. A., Jansen, R. A., Windhorst, R. A., Odewahn, S. C., & Hibbard, J. E. 2005, *ApJ*, 630, 784
- Tortora, C., Napolitano, N. R., Cardone, V. F., et al. 2010, *MNRAS*, 407, 144
- Tremonti, C. A., Heckman, T. M., Kauffmann, G., et al. 2004, *ApJ*, 613, 898
- Tresse, L., Rola, C., Hammer, F., et al. 1996, *MNRAS*, 281, 847
- van den Bosch, F. C., Aquino, D., Yang, X., et al. 2008, *MNRAS*, 387, 79
- van der Wel, A. 2008, *ApJL*, 675, L13
- Veilleux, S., & Osterbrock, D. E. 1987, *ApJS*, 63, 295
- Veron, P., Goncalves, A. C., & Veron-Cetty, M.-P. 1997, *A&A*, 319, 52
- von der Linden, A., Wild, V., Kauffmann, G., White, S. D. M., & Weinmann, S. 2010, *MNRAS*, 404, 1231
- Wang, L., Li, C., Kauffmann, G., & De Lucia, G. 2007, *MNRAS*, 377, 1419
- Weinmann, S. M., Kauffmann, G., van den Bosch, F. C., et al. 2009, *MNRAS*, 394, 1213
- Weinmann, S. M., Kauffmann, G., von der Linden, A., & De Lucia, G. 2010, *MNRAS*, 406, 2249
- Weinmann, S. M., van den Bosch, F. C., Yang, X., & Mo, H. J. 2006, *MNRAS*, 366, 2
- Wetzell, A. R., Tinker, J. L., & Conroy, C. 2012a, *MNRAS*, 424, 232
- Wetzell, A. R., Tinker, J. L., Conroy, C., & van den Bosch, F. C. 2012b, *MNRAS*, 432, 336
- Williams, R. J., Quadri, R. F., Franx, M., van Dokkum, P., & Labbé, I. 2009, *ApJ*, 691, 1879
- Woo, J., Dekel, A., Faber, S. M., et al. 2013, *MNRAS*, 428, 3306
- Wyder, T. K., Treyer, M. A., Milliard, B., et al. 2005, *ApJL*, 619, L15
- Yan, R., Newman, J. A., Faber, S. M., et al. 2006, *ApJ*, 648, 281
- York, D. G., Adelman, J., Anderson, J. E., Jr., et al. 2000, *AJ*, 120, 1579
- Zabludoff, A. I., Zaritsky, D., Lin, H., et al. 1996, *ApJ*, 466, 104
- Zibetti, S., Charlot, S., & Rix, H.-W. 2009, *MNRAS*, 400, 1181